Annual Sediment Transport Dynamics in the Narayani Basin, Central Nepal: Assessing the Impacts of Erosion Processes in the Annual Sediment Budget

Guillaume P. Morin, Jérôme Lavé, Christian France-Lanord, Thomas Rigaudier, Ananta Prasad Gajurel, Rajiv K Sinha

Annual sediment transport dynamics in the Narayani basin, Central Nepal: assessing the impacts of erosion processes in the annual sediment budget

Guillaume Morin[1*], Jérôme Lavé[1], Christian France-Lanord[1], Thomas Rigaudier[1], Ananta Prassad Gajurel[2], Rajiv Sinha[3]

[1] Centre de Recherches Pétrographiques et Géochimiques (CRPG), UMR 7358 CNRS-Université de Lorraine, 15 rue Notre Dame des Pauvres, F-54500 Vandœuvre-lès-Nancy, France

[2] Department of Geology, Tribhuvan University, Ghantaghar, Kathmandu, Nepal

[4] Department of Earth Sciences, Indian Institute of Technology, Kanpur 208 016, India

[*] Corresponding author: G. P. Morin: guillaume.p.morin@gmail.com, now at Laboratoire d'Océanographie de Villefranche sur Mer (LOV), UMR 7093, CNRS/UPMC, F-06230 Villefranche-sur-Mer Cedex, France.

Corresponding author: G. P. Morin: guillaume.p.morin@gmail.com,

*now at Laboratoire d'Océanographie de Villefranche sur Mer (LOV), UMR 7093, CNRS/UPMC, F-06230 Villefranche-sur-Mer Cedex, France.

Key Points:

- Erosion in Central Nepal is supply-limited and driven by monsoonal precipitation, which controls triggering of landslides.
- Glacial and soil erosion are minor in the annual sediment budget compared to landslides.
- Current erosion rates agree with long-term erosion rates, suggesting efficient buffering of these drainage systems.

This article has been accepted for publication and undergone full peer review but has not been through the copyediting, typesetting, pagination and proofreading process which may lead to differences between this version and the Version of Record. Please cite this article as doi: 10.1029/2017JF004460

Abstract

Identifying the roles of erosional processes in the denudation of mountain ranges requires a better understanding of erosional sensitivity to climatic, topographic, or lithologic controls. We analyzed erosion in the Narayani River basin (draining central Nepal, and presenting contrasted lithologic and geochemical signatures in its outcropping rocks, and a wide variety of erosional processes and climatic conditions) to assess the relative contributions of erosion processes to the annual sediment export. By combining ADCP measurements with depth profiles and daily surface samplings of the suspended load, we propose a simplified model to precisely calculate sediment fluxes at the basin outlet. We estimate an equivalent erosion rate of $1.8^{+0.35}_{-0.2}$ mm/yr for the year 2010, similar to the average value of $1.6^{+0.35}_{-0.2}$ mm/yr estimated from 15 years of records and long-term (~ky) denudation rates of 1.7 mm/yr derived from cosmogenic nuclides. The stability of erosion is attributed to efficient buffering behavior and spatial integration in the drainage system. Strong relations between rainfall events and the sediment export suggest that the system is mainly supply-limited. Combining physical calculation of sediment fluxes with grain size analyses and geochemical tracers (hydroxyl isotopic compositions, carbonate contents, and total organic carbon content), we estimate that glacial and soil erosion do not contribute more than 10% and a few %, respectively to the total budget, and are only detectable during premonsoon and early monsoon periods. During the monsoon, erosion by landslides and mass-wasting events overwhelms the sediment budget, confirming the dominant role of these erosional processes in active mountain chains.

1. Introduction

Mountain range landscapes and topography result from tectonic deformation and mass removal by erosion. The effects of tectonics and climate in shaping topography depend largely on the erosive processes acting at the Earth's surface and their sensitivity to these forcings. Such erosive controls have implications at all time scales and are particularly relevant to the long-standing debate on the interactions between tectonics, climate, and erosion during orogenic construction. Comprehension and quantification of such interactions is challenging, in part due to the diversity of erosive processes (hillslope, fluvial, glacial) that occur in different parts of the landscape and are variously sensitive to climatic variables (e.g., Avouac, 2003; Gabet et al., 2004b; Bookhagen et al., 2005; Champagnac et al., 2012; Fuchs et al., 2015; Deal et al., 2017).

Because of its sustained tectonic activity and diversity of climatic conditions, the Himalayan range is a remarkable region of the world for studying the interactions between active tectonics, climate, and topography (e.g., Lavé & Avouac, 2001; Burbank et al., 2003; Clift et al., 2008; Gabet et al., 2008; Godard et al., 2014; Deal et al., 2017). The topographic step between the low Ganga plain and the highest Himalayan summits or the Tibetan Plateau acts as a barrier to atmospheric circulation and drives heavy precipitation during the Indian monsoon (Boos & Kuang, 2010; Molnar et al., 2010). Monsoonal precipitation combined with the steep Himalayan relief produces denudation rates among the highest on Earth. The system generates one of the most important sediment fluxes on the planet, feeding the Ganga plain and the Bengal fan.

Understanding how Himalayan topography and tectonics respond to climatic and erosive forcings requires a comprehensive view of active erosion in the Himalaya. This includes studying present erosional fluxes, documenting the dominant erosional processes occurring in different physiographic units of the range, and defining the response of these erosional processes to climatic forcing.

Among erosional processes, landslides have been shown to be the major erosive agent in active mountain ranges (Hovius et al., 1997; Dadson et al., 2004; Parker et al., 2015) and particularly in Himalaya, where their occurrence displays high spatial and temporal variability (Shroder, 1998). The factors that control their distribution, evolution, and behavior may be as diverse as earthquakes (Dadson et al., 2004; Meunier et al., 2008), rainstorms (Iverson, 2000; Gabet et al., 2004a), or accumulated seasonal rainfall through groundwater

saturation (Gabet et al., 2004b; Dahal & Hasegawa, 2008) which affects bedrock strength and hillslope angle of repose (Gabet et al., 2004a) as suggested by the coincident scaling of topography and precipitation observed in the steep relief of the Greater Himalaya.

Soil erosion may also play a significant role as suggested by Heimsath et al., (2012) and Larsen et al., (2014) who reported that soil production rates can be very high (up to 2.5 mm/yr) and increase to above theoretical limits with physical erosion in rapidly eroding watersheds (e.g., Gabet & Mudd, 2009). Nonetheless, those authors also reported that soil production rates represent only a fraction of catchment-wide denudation, which is largely dominated by mass wasting and landslides at the mountain scale. While in the Middle Hills of central Nepal, south of the high range, (West et al., 2015) identified that soil erosion can dominate physical erosion at the catchment scale in the absence of active landslides, such that the dominance of landslides over soil erosion remains to be shown at the scale of the entire range.

Lastly, glacial erosion is potentially more efficient than landslide erosion driven by fluvial incision (e.g., Hallet et al., 1996), although this inference was recently questioned (Thomson et al., 2010). Yet, the High Himalayan summits are covered by numerous glaciers and large U-shaped valleys of up to 3,000 m relief that attest to past glacial erosion so that Gabet et al., (2008) proposed that glacial erosion dominates in rivers draining the northern sides of the range in central Nepal, although this contribution is dwarfed by other contributions at the scale of the range because of the limited extent of glacier cover. In contrast, (Godard et al., 2012) concluded from ^{10}Be concentrations in river sands collected in the same area that active glacial erosion can exceed the long-term erosion rate by two or three times, which leaves an imprint in downstream river sediments.

In that respect, the aim of this study is to measure the intensity of erosion and assess the relative contributions of the different erosion processes at the scale of the Himalayan range. We followed an alternative and integrative approach by studying the sediment export of a major river during an entire monsoon cycle. We characterized the fluxes and sources of the sediment transported by a major river and their relations with rainfall and temperature chronicles in central Himalaya, a region marked by strong rainfall seasonality. We explore the relative contributions and intensities of the different erosion processes in relation to climatic variables. Rather than monitoring a large number of watersheds exposed to contrasted climates and erosional processes, our approach offers the possibility of tracking

the imprint of diverse sediment sources in the same system and their responses to the seasonality of the monsoon climate.

Sediment transport in a large river and associated sedimentary bodies might result in a dampening / delaying of the original signals associated with a change in climatic or tectonic signal (Covault et al., 2010; Armitage et al., 2011; Coulthard & Van de Wiel, 2013) due to internal dynamics (Jerolmack & Paola, 2010) or the timescale of integration (Castelltort & Van Den Driessche, 2003; Armitage et al., 2011). In order to catch the initial signal, the filter associated to the sediment transport has to be limited as much as possible, for example by monitoring the sediment at the outlet of the mountain basin and before the plains. See Romans et al., (2016) for extensive review.

Hence, our method consists of analyzing the sediment load of a large river system at its outlet from the mountain range. This method offers several advantages: 1) it spatially smooths the stochastic effects of landslide mass wasting; 2) it provides an overall view on the erosion of a whole Himalayan section, including glaciated high peaks; and 3) it yields a direct interpretative framework of the chemical composition and sedimentological characteristics of sediments transported further downstream, which could help to decipher the sedimentary records of the Indo-Gangetic foreland basin or Bengal fan.

This paper focuses specifically on estimating the current physical erosion rate and its recent evolution in the Narayani River basin, one of the major rivers draining and eroding central Himalaya, and assessing the yields of each erosional process in the sediment budget. To do so, we analyzed sediment concentration chronicles, the geochemical composition of riverbanks and suspended loads, and hydrologic and meteorological datasets along the Narayani River. We present an original dataset of daily surface suspended sediment sampling from May to October 2010, a period that encompasses premonsoon, monsoon, and postmonsoon periods and about 80% of the total annual rainfall. We assess current rates of erosion by combining this dataset with occasional sediment depth sampling and an acoustic Doppler current profiler (ADCP) current velocity survey acquired during the 2011 monsoon, which allows us to build a semi-empirical model of sediment transport that integrates sediment fluxes over the river depth. We apply our model to suspended load concentration data recorded by the Department of Hydrology and Meteorology of Nepal (DHM) to document erosion rates over the past decade, which we then compare to current erosion rates reported by (Andermann et al., 2012a) and long-term denudation rates determined by cosmogenic dating (Godard et al., 2012, 2014; Lupker et al., 2012a).

Our 2010 sediment dataset includes tracers to discriminate between sediment sources, for instance grain size and geochemical characteristics including carbonate content, the hydrogen isotopic composition of hydrated silicates, and total organic carbon content. Thus, we present a multivariate analysis of the suspended load in 2010 that reveals geochemical fluctuations in relation to sediment flux and river discharge. These temporal variations are likely related to the contributions of the different erosion processes active in the basin, i.e., mainly glaciers, soils, and landslides.

2. Geologic, climatic, and geomorphologic settings

The Narayani River drains the central Nepal Himalayan range and is the most important tributary of the Ganga in terms of discharge and sediment flux (Singh et al., 2008; Andermann et al., 2012a; Lupker et al., 2012a). It drains a 32,000 km^2 mountain basin whose elevation varies from 180 to 8147 m. The drainage system comprises five major tributaries from west to east: Kali Gandaki, Seti, Marsyandi, Bhuri Gandaki, and Trisuli. The Kali and Trisuli Rivers drain a part of the Tibetan plateau that corresponds to 39 and 40% of their respective basin areas. The Narayani basin drains 5 main Himalayan geologic units from north to south: 1) the Tethyan Sedimentary Series (TSS), a low-grade Palaeozoic–Eocene sedimentary series of the passive northern Indian margin that includes a large proportion of limestone and carbonates; 2) the High Himalayan Crystalline (HHC) formations, high-grade metamorphic gneisses and migmatites; 3) the High Himalayan Leucogranite (HHL), intrusive into the HHC and TSS; 4) the Lesser Himalaya (LH) formations, variably metamorphosed Indian crust material of Precambrian to Palaeozoic age; and 5) the Mio-Pliocene Siwaliks, sediments of the foreland basin exhumed by the most recent frontal thrusts (Colchen et al. 1986). According to the geologic map (Department of Mines and Geology of Nepal), the respective surface proportions of outcropping lithologies drained by the Narayani basin are ~30% TSS, ~24% High Himalayan gneisses and leucogranites (HHC+HHL), and ~46% LH units. Finally, the surface area of the Siwaliks units drained by the Narayani basin upstream of Narayanghat is negligible.

The Narayani basin is highly exposed to the monsoon, which generates a flooding season between mid-June and mid-to-late September that represents around 80% of the 1,400–1,900 mm/yr mean annual rainfall (Shrestha, et al., 2000; Bookhagen and Burbank, 2010; Andermann et al., 2011, 2012b). During the monsoon, northwestward winds bring moisture generated at the surface of the Bay of Bengal to the mountain range, generating intense

orographic precipitations. Rainfall in the Narayani basin varies greatly, with annual rainfall ranging from <50 mm in the Mustang area (the most NW part of the watershed) to ~5,000 mm south of the Annapurna Massif (Putkonen, 2004). In central Nepal, the morphologic transition from the Lesser Himalaya lowlands and Middle Hills to the High Himalaya is characterized by a sharp break in slope that forms the principal orographic barrier and stops monsoon clouds at a ~4,000 m elevation.

Consequently, the High Himalayan foothills region receives the most precipitation in Nepal (Anders et al., 2006; Bookhagen & Burbank, 2006, 2010; Andermann et al., 2011). In the Narayani basin this effect is enhanced by the relatively low elevation of the frontal Mahabharata Range, which favors cloud penetration into the interior of the range and probably explains the precipitation in front of the Annapurna Massif that is more intense than anywhere else in central Nepal. Because of the orographic barrier, the northern part of the watershed is very arid.

The High Himalayan range includes several of the highest summits in Nepal and is exposed to snowfall (up to 1 m of equivalent water) mostly during the winter (Putkonen, 2004). Glaciers cover most of the principal massif and represent ~9% of the Narayani watershed area (GLIMS database). Snow and glacier melt waters are estimated to contribute around 10% of the annual Narayani discharge (Bookhagen & Burbank, 2010; Andermann et al., 2012b). Although snow/glacier melt peaks in early July, its influence is most noticeable in the river discharge during the premonsoon period (Immerzeel et al., 2009; Bookhagen & Burbank, 2010).

The contrasted N-S pattern of precipitation directly influences the distribution of incision and erosion along Himalayan valleys (LavÉ & Avouac, 2001). Late Holocene erosion rates may reach up to 3–5 mm/yr in the High Himalaya (Godard et al., 2012), whereas the Lesser Himalaya is characterized by subdued erosion rates between 0.1 and 0.5 mm/yr (Godard et al., 2014). In the High Himalaya, the present snowline is above 5,000 m elevation, which limits the extent of active glacial and peri-glacial erosion, but large open U–shape valleys extending down to 3,000 m attest to efficient glacial erosion during glacial stages. In the northernmost part of the basin, the relief is lower than in the High Himalaya, and erosion rates are very low, around 0.1 mm/yr, consistent with the arid conditions there (Gabet et al., 2008).

Sediments are efficiently transported by the main tributaries of the Narayani River, as suggested by numerous bedrock-floored channel segments across the High Himalaya and across the Mahabharata hills upstream of the Main Boundary Thrust. Nevertheless, the

presence of large and thick fluvial or debris-flow terraces in the Lesser Himalaya (Iwata et al., 1984; Fort, 1987; Fort et al., 2010; Lavé & Avouac, 2000) attest to periods of episodic and extensive alluviation in the lower valleys of the Narayani basin. The presence of these sediment reservoirs has been considered to introduce a potential lag in the Himalayan sediment routing and a delay between the erosion signal and the effective export (Blöthe & Korup, 2013). However, at the scale of the Marsyandi River, the contribution of LH terraces to the present sediment budget is considered negligible because of their relatively old age of formation (Attal & Lavé, 2006). Therefore, we consider that the buffer effect exerted by terraces is minor compared to the total sediment flux, and that most sediments are exported upon reaching the active drainage system.

Finally, at the scale of the Narayani watershed, recent studies have estimated the annual suspended load flux to be 130^{+220}_{-70} Mt/yr (Sinha & Friend, 1994; Andermann et al., 2012a) and, based on ^{10}Be cosmogenic nuclides in river sands, the late Holocene erosive flux between 110 and 184 Mt/yr (Lupker et al., 2012a). Such fluxes correspond to mean denudation rates of 1.2–2.2 mm/yr.

3. Sampling and methods

3.1 Study area

We sought to perform sediment sampling and ADCP on a single and narrow channel tread, i.e., upstream of the braided morphology SW of Narayanghat (Fig. 1). Thus, our choice of study areas was limited to the Narayani River ~5km downstream from the confluence of the Kali and Trisuli Rivers, just upstream of the Narayanghat bridge (27.700ºN, 84.421ºE; Figs. 1 and S1). The bridge is located ~3 km downstream from a DHM gauging station that has been reporting Narayani River water level data since 1963 (DHM/FFS, 2004), including hourly water levels for 2010 and 2011 (online dataset of DHM website) and daily suspended load measurements. However, this last chronicle is relatively discontinuous and does not include a description of sediment concentration with depth, which justified a more thorough study with depth sampling in 2011.

In front of the DHM station, the Narayani channel is relatively deep (15–20 m depth) and narrow (170–190 m wide) and the river is embanked in cemented river terraces and Siwalik sandstones. In the Narayanghat bridge segment, the river is bordered by pebbles and a sandy beach on the right bank and partly constrained concrete structures on the left bank.

Downstream of Narayanghat, the river flows through the Chitwan Dun where the channel widens from 230 to 330 m and presents large sandy or pebbly alluvial bars and smoother riverside slopes. In the study area, Narayani River bedload material comprises coarse pebbles and is only exposed along these alluvial bars (see supporting Table S2; (Mezaki & Yabiku, 1984; Attal & Lavé, 2006; Dingle et al., 2016)).

3.2 ADCP velocity distribution and discharge measurements

We measured river discharge via cross-channel ADCP transects near the DHM gauge station and immediately upstream of the Narayanghat bridge (Fig. 1). To be representative, ADCP discharge measurements (and depth samplings, section 3.3) were performed in the area immediately upstream of the bridge because the hydrodynamic conditions there might be considered analogous to those during the daily DHM suspended load samplings. We measured the current velocity distribution in the water column following procedures proven on large rivers (Filizola & Guyot, 2004; Lupker et al., 2011a). A RD Instruments 1200 kHz Rio Grande ADCP was coupled to a Tritech 200 kHz PA200 echosounder to accurately detect the river bottom and a Garmin eTrex H GPS to ensure an absolute reference of displacement. The system was mounted on the side of a motorized rubber boat from IIT Kanpur. Current velocity measurements were acquired every 420–675 ms with a vertical resolution (or bin size) of 43–67 cm depending on the instrument's configuration. Raw and processed data were exported with the Teledyne WinRiver software and post processing was performed using R software. Step-by-step treatments of water discharges are reported in sections 4.1.1 and supporting Text S6, and sediment flux calculations in sections 4.2.3 and supporting Text S7. Note that we continuously recorded water velocity during depth sampling (section 3.3) to assess hydrodynamic conditions and river bottom topography at the moment of sampling.

3.3 Sediment sampling

Our sediment dataset includes 1) depth sampling to constrain the concentration and properties of sediments throughout the water column, 2) daily samplings at the river surface during the 2010 monsoon and 3) samples of bank and suspended load from tributaries of the Narayani river and glaciers in the Marsyandi and Langtang Valleys, to characterize geochemical composition of erosion agents and provenance of the sediments. The distribution of the suspended load concentration $Cs(z)$ in the water column is generally nonuniform and depends on the sediment concentration at the bottom, water depth, hydrodynamic conditions, and

sediment characteristics including grain size and mineral properties (i.e., density and shape factor) (Garcia, 2008). Depth profiles were performed to evaluate the bias on sediment discharge when *Cs* is considered homogeneous over the entire section or based solely on surface samples. Six profiles were realized during the 2005, 2007, and 2011 monsoons. Each depth profile sampled in 2005 consisted of seven samples, and an additional triple sampler close to the riverbed was used in 2007 to document the boundary layer between the bedload and suspended load. We used the sediment depth sampling method described in (Lupker et al., 2011b). The sediment depth sampler consists of a 5 L tube open at both ends and a closure system actuated by a compressed air system and monitored from the boat. The boat was left drifting on the axis of the river in full current and the sampling bottle, ballasted by a 20 kg weight, was submerged to the desired depth and stabilized to ensure near isokinetic sampling conditions. The exact sampling depth was obtained using a pressure gauge fixed on the sampler. The sampler was closed from the boat by the compressed air system while the GPS position, depth, and ADCP data were recorded. The triple-sampler used in 2007 consists of three 1 L horizontal Niskin bottles, mounted 50 cm apart on a ballasted rigid frame, that were pneumatically closed when the sampler touched the bottom.

In 2011 we sampled water and sediments along depth profiles while the ADCP was left running. For each profile, four samples were taken at regular depth intervals along the high-flow axis of the river to account for vertical variability of the suspended load concentration in the river section. To assess lateral variability of the sediment load along a transversal river section at high stage, one depth profile was sampled off-axis on 6 August 2011.

Once retrieved on board, the sampler was kept sealed until the boat reached a riverbank. The samples were then transferred into opaque plastic bags with special care to avoid any loss of material. Samples were stored in the bags until filtration within 6 to 48 h after collection. The total water + sediment samples were weighed and filtered through 90-mm-diameter 0.22 µm Poly Ether Sulfone filters in a pressurized Teflon-coated filtration unit. The sediment concentration was calculated by dividing the dried sediment weight by the weight of the water. The overall uncertainty on sediment concentrations is 10^{-3} g/L.

Surface sediment sampling was performed at 0800 local time every four days from 19 May to 16 June, then daily until 10 October 2010, from the center of the Narayanghat bridge (27.699963°N, 84.418537°E; Figs. 1 and S1) where river flow is maximum. Duplicate one-liter samples were collected in an open bottle ballasted with a 10 kg weight. This sampling

period and frequency fully covered the monsoon season, allowing us to capture about 80% of the annual sediment discharge. Surface sediment samples were weighed and filtered following the method described above for the depth profiles.

Finally, the suspended load is independently sampled at the DHM station following USGS methods (DHM, 2003) on a daily basis during monsoons and once a week otherwise. This dataset, made available by the DHM for 14 years (1976–1977, 1979, 1985–1986, 1993, 2001–2005, and 2010–2012), complements our dataset during the winter and allows us to calculate average sediment fluxes over decades. Their exact sampling protocol has not been provided except that initial samplings were performed with a depth-integrative USGS bottle, whereas samples of the last decade have been taken at the surface from a small overhanging cliff on the left riverbank.

3.4 Grain size and geochemical analyses

River sediments were analyzed to document the grain size and chemical characteristics of the suspended load and track its origin during the 2010 monsoon. After filtration, sediment samples were freeze-dried and removed from the filters. The samples were weighed and quartered with a splitter to obtain representative aliquots for further grain size and chemical analyses. Special care was taken to preserve the integrity of the samples during all these steps. Sample aliquots dedicated to chemical analyses were powdered in an agate mortar using a Retsch grinder.

Particle-size distributions from 0.1 to 875 µm were obtained using a Sympatec HELOS/BF laser granulometer with a SUCELL wet disperser (LIEC, Nancy, France). Prior to analysis, samples received a 30-s ultrasonic treatment to break-up mineral clusters and aggregates, but we avoided chemical pre-treatments (e.g., HCl or hydrogen peroxide, generally used to remove carbonates or organic matter) to preserve unstable mineral phases. Prior analyses of major and trace element compositions at SARM-CRPG (Nancy) did not identify any discriminant tracers of the sediment origin, as expected by the predominance of metasediments outcropping in the Himalaya. Instead, we used carbonate content and carbon and oxygen isotopic compositions, total organic carbon (TOC) content and carbon isotopic composition, and the hydroxyl content and D/H of the silicate fraction as specific tracers.

Carbonate content and carbon isotopic compositions were measured by phosphoric acid dissolution at 70 °C on a gas-bench coupled to a Thermo Scientific MAT 253 stable isotope

ratio mass spectrometer (IRMS). We corrected for analytical fractionation, and overall uncertainty is ±0.9% for carbonate content and under ±0.2‰ for carbon isotopic compositions (measured relative to Pee Dee Belemnite, PDB, as $\delta^{13}C$ (‰) = $[(^{13}C/^{12}C)_{sample}/(^{13}C/^{12}C)_{PDB} - 1] \times 1000$). Carbonate content and carbon and oxygen isotopic compositions in the 2010 surface suspended load samples were also measured in 30–50 mg aliquots by classical phosphoric acid dissolution on a manual vacuum extraction line, allowing chemical separation and quantification of calcite and dolomite (A. Galy & France-Lanord, 1999; Sheppard & Schwarcz, 1970). The isotopic compositions of calcite and dolomite were measured from the released CO_2 by a modified VG 602 mass spectrometer and are reported as $\delta^{18}O$ (measured relative to Vienna Standard Mean Ocean Water, VSMOW, as $\delta^{18}O$ (‰) = $[(^{18}O/^{16}O)_{sample}/(^{18}O/^{16}O)_{VSMOW} - 1] \times 1000$) and $\delta^{13}C$ with reproducibilities of ±0.1‰.

TOC concentrations and carbon isotopic compositions were measured using an elemental analyzer coupled to an Elementar IsoPrime IRMS after carbonate dissolution by diluted hydrochloric acid digestion following (Galy et al., 2007). TOC is reported in wt% of the decarbonated sediment. Overall reproducibilities for TOC and $\delta^{13}C$ measurements are 0.02 wt% and 0.25‰, respectively.

Low-temperature plasma ashing has been successfully used to remove hydrogen-bearing carbon compounds from a mix with mineral particles by oxidizing the organic matter (Miller et al., 1979; Pike et al., 1989; D'Acqui et al., 1999; Lebeau et al., 2014). This method was tested on Narayani sediment but was unnecessary in our case. Therefore, hydroxyl content, $[H_2O^+]$, and D/H isotopic compositions were analyzed after pre-dehydration at 120 °C under vacuum for 48 h following methods described in (Lupker et al., 2012b; Bauer & Vennemann, 2014). Hence, the water analyzed here is mainly composed of hydroxyls linked to mineral particles (micas and clays) and minor amounts of iron hydroxides and other hydrated minerals. This includes primary water inherited from the metamorphic source rock and secondary water due to hydration during weathering reactions. D/H is reported relative to VSMOW as δD (= $[(D/H)_{sample}/(D/H)_{VSMOW} - 1] \times 1000$). The overall reproducibility on sediments and rocks is 2‰ for δD and 0.1% for $[H_2O+]$ (Sharp & Atudorei, 2001; Garzione et al., 2008; Lupker et al., 2012b).

Grain size, carbonate content, and TOC were measured for each sample, whereas hydroxyl and major/trace element contents were analyzed for one third of the samples because of cost limitations.

4. Results

4.1 Water discharge and hydroclimatic record

4.1.1. ADCP discharge calculation and comparison to DHM record

Although ADCP measurement is a relatively standard technique, operating on the Narayani River was challenging for several reasons. Hence, the ADCP current velocity dataset acquired during the 2011 monsoon showed inconsistencies due to technical limits during high flow conditions. High current velocities, as high as 7 m/s (32 km/h), made it difficult to maintain the boat trajectory perpendicular to the flow. Despite employing a narrow-solid-angle echo sounder to detect the channel bottom, we recorded important inconsistencies marked by unrealistic spikes in the topographic profile. We suspect areas of high turbulence and vertical eddies, highly concentrated sediment plumes near the river bottom, or large drifting objects (e.g., logs) to have induced these bottom-detection anomalies (Fig. 2a, top). Data were exported with the WinRiver software but discharges were underestimated due to the anomalies. Hence, the data were numerically post-treated with R software. To derive water velocities over the whole section and compute water discharge, we corrected the bottom-detection errors to a realistic topography and filled the missing velocity data by fitting a law of the wall to the top ~1.2-m layer blind to the transducer and the 0.5-m-thick bottom layer in the ADCP raw image (Fig. 2a, see supporting Text S6 for correction details). Double integration of the corrected velocity section over the local water depth and across the section provides the discharge value *Q*.

After correction, ADCP-derived discharges are in good agreement with discharges reported by the DHM station 3 km upstream (Fig. 2b). DHM discharges are converted from hourly water level reports using a rating curve. Although discharges varied from 4,500 to 7,500 m^3/s during our 4-day campaign, the twelve ADCP discharge values differ by <5% from the DHM values.

ADCP data were acquired during depth sampling in the beginning of August 2011, when the monsoon is well established and the river is continuously at a high stage. Although our direct

observations missed the most extreme floods (Q > 10,000 m^3/s), they document Narayani River discharges within the upper 25% of the DHM daily record since 1962 (supporting Figure S2). We thus consider that our observations well document sediment transport during moderate floods, which are more frequent than larger floods and cumulatively transport most of the annual sediment export (Wolman & Miller, 1960; Andermann et al., 2012a).

4.1.2. Flow separation, snow/ice melt, and the hydroclimatic record

During the monsoon period, relating climatic variables to the evolution of sediment fluxes and their origins requires rainfall and temperature chronicles over the entire watershed. Eighty DHM weather stations document daily average precipitation in the Narayani basin (supporting Figure S4), but they are heterogeneously distributed over the watershed with more stations along the Lesser Himalaya and along valley thalwegs. This over-representation of weather stations along valley bottoms compared to ridges and crests was identified as a possible source of bias by (Burbank et al., 2003).

To circumvent this potential bias, we exploit the fact that, in most flow separation models, river hydrographs can be separated into two main components: runoff and baseflow. The baseflow component *Qb* represents the contribution from groundwater reservoirs that slowly responds to rainfall events, and the direct runoff or storm runoff component *Qd* represents the sum of infiltration and saturation excess overland flow and is characterized by short response and transfer times after rainfall events. In this region, (Andermann et al., 2012b) demonstrated that direct runoff represents a minor part of the river discharge during the monsoon period (~25%) although it exerts a major control on sediment fluxes exported from the mountain basins (Andermann et al., 2012a). We used flow separation to assess Andermann et al., (2012a)'s conclusions and isolated direct runoff for the year 2010. Furthermore, we estimated snow/ice melt to determine the contribution to runoff from high altitude areas, and hence the amount of sediment potentially coming from glacial erosion. We then compared these fluxes with geochemical tracers to decipher the erosion processes involved.

Many digital filters have been proposed to separate the river hydrograph components (e.g., (Arnold et al., 1995; TG Chapman et al., 1996; Arnold & Allen, 1999; Chapman, 1999; Wittenberg & Sivapalan, 1999; Furey & Gupta, 2001), but those developed by (Eckhardt, 2005, 2008) were efficiently applied to natural basins (Andermann et al., 2012a; Tolorza et al., 2014; Struck et al., 2015). More specifically in Nepal, Andermann et al. (2012b) used generic digital filters based on daily discharges adapted from (Eckhardt, 2005), setting the

recession constant a to 0.98 and the ratio of annual baseflow to annual streamflow BFI_{max} to 0.8 for all studied rivers. Here, to separate the 2010 Narayani hydrograph, we used the same digital filter (Fig. 3a), but set BFI_{max} to 0.75 to improve hydrograph fitting. The recession phase of the hydrograph during the postmonsoon period (beginning on Julian day 266 in 2010) slightly departs from an exponential curve: we accounted for this difference by varying a nonlinearly between 0.987 at low baseflow and 0.91 at the highest baseflow. We also adapted (Eckhardt, 2008)'s filter to the hourly discharge dataset by replacing the daily coefficient a by its hourly counterpart $a^{1/24}$.

Integration of the 2010 daily discharge dataset provides annual Narayani discharge Q_{total} = 48.1 km^3/yr, annual direct runoff Qd_{total} = 11.5 km^3/yr (~24% of Q_{total}), and annual baseflow Qb_{total} = 36.6 km^3/yr (76% of Q_{total}, coherent with BFI_{max} set at 0.75). These figures are in close agreement with previously reported values (Andermann et al., 2012b).

The direct runoff component closely follows the daily precipitation in the Narayani basin from early July until the end of the monsoon (Fig. 3b). During the premonsoon period in May and early June (Julian days 100–165), the discrepancy observed between rainfall and direct runoff indicates that a significant amount of water does not readily reach the streamflow. Several explanations likely contribute: 1) a certain amount of water is lost to evaporation because evapotranspiration is at its maximum during late spring (Bookhagen & Burbank, 2010; Andermann et al., 2012b); 2) a part of the precipitation may fall as snow, delaying the direct runoff response to rainfall; and 3) a certain amount of runoff infiltrates the ground surface as hypodermic flow to increase soil moisture when deeper water enters an aquifer as groundwater (Andermann et al., 2012b).

Finally, it has to be noted that the calculations described above cannot separate the rain and ice/snow melt flow components. If we assume that a major fraction of glacial meltwater is efficiently channelized and rapidly joins the river network, ice melt should contribute to the direct runoff rather than the groundwater component. Conversely, melting of the snow pack during the spring will rather infiltrate the ground and join the groundwater component. Hydrological modeling in the Dudh Kosi basin in Eastern Nepal (Nepal et al., 2014) suggests roughly equal partitioning between snow and ice melting in the hydrologic budget of that basin. For 2010, based on the DHM daily temperature records, the surface extent of glaciers (GLIMS Glacier Database) and SRTM topographic data, and based on a positive degree day model (PDD value or melt factor of 7 mm/°C/day for clean ice/snow and 4 mm/°C/day for debris covered ice below 5,000–5,200 m; (Kayastha et al., 2000; Wagnon et al., 2007 ;

Racoviteanu et al., 2013)), we estimate the total snow/ice-melting contribution to be ~8% of the annual Narayani discharge, with a peak contribution to the daily discharge of <10% during July (Fig. 3). Given this limited contribution, including snow/ice melt marginally modifies our flow separation data during the monsoon period (supporting Text S10).

4.2 Suspended load and sediment fluxes

4.2.1. Daily surface concentrations

Our suspended load concentration at the surface Cs_0 data is in overall good agreement with DHM measurements (supporting Figure S5). Except for the recession period at the end of September during which our data are systematically higher than the DHM data, more than two thirds of the datasets differ by less than 50%. More importantly, the slope of the correlation between the two datasets is very close to one (1.02, or 1.18 excluding the two main outliers). This suggests that lateral turbulent mixing of surface sediments between the central part of the channel and the riverbanks is relatively efficient, leading to a roughly uniform concentration increase with depth across the river section. Although the DHM sampling point is on the left bank of the Narayani only 1.8 km downstream from the confluence of the Kali Gandaki and Trisuli Rivers, the DHM record does not seem to be substantially impacted by incomplete mixing between the suspended load of these two contributing rivers, and is a priori representative of the entire Narayani watershed.

Temporal variations of Cs_0 (Table 1) during the 2010 monsoon roughly follow the river hydrograph (Fig. 3). Cs_0 is quite low during the premonsoon period, and starts exceeding 1 g/L when monsoonal precipitation begins in mid-June (Julian day 166) and the Narayani discharges rises above 1,000 m^3/s. During the monsoon, i.e., until mid-September (~Julian day 260), Cs_0 variations roughly mimic discharge variations, including reduced flow periods around mid-August (Julian days 217–230) and flood peaks of intense direct runoff events corresponding to Cs_0 increases above 4–8 g/L. When precipitation stops in the postmonsoon period, Cs_0 rapidly drops to values <0.5 g/L, whereas direct runoff decreases slowly.

Throughout the course of one year, suspended sediment Cs_0 plotted against daily Narayani discharge Q displays a clockwise hysteresis loop (Fig. 4a) interpreted as dilution by the increased contribution of groundwaters discharging into the streamflow at the climax and until the end of the monsoon (Andermann et al., 2012a; Tolorza et al., 2014). In 2010, this

period corresponded to late July to mid-September (Julian days 210–260) during which *Qb* was above 2,500 m^3/s and represented almost all of the total Narayani discharge.

As proposed by (Andermann et al., 2012a) for several Himalayan rivers, the sediment load-discharge hysteresis is reduced or eliminated when the groundwater discharge component is removed from the total discharge, i.e., when Cs_0 is displayed versus the direct runoff component *Qd*. During the 2010 monsoon, our data
confirm their observation and display a rough positive relationship between Cs_0 and *Qd* (Fig. 4b, c).

4.2.2. Suspended sediment distribution in the water column

Vertical sampling profiles obtained in 2005, 2007, and 2011 display Cs_0 values ranging from 1.4 to 4 g/L, with an average of 2.44 g/L (Table 1, Fig. 5).

Sediment concentration increases with depth in the 2011 profiles whereas the 2007
concentration profile is almost uniform, although it was sampled at a lower discharge (~3,000 m^3/s).
Due to high flow conditions in 2011, dredging bedload samples would have required a much heavier version (Edwards & Glysson, 1999) of our original Helley Smith bedload sampler. Nonetheless, former depth profiles sampled in 2005 and 2007 (PB and LO, respectively) with a bottom triple-sampler provide constraints on the bottom suspended and bedload concentrations. As expected, bottom samples PB54 and LO758C show very high concentrations of 10.24 and 30.90 g/L, respectively, illustrating the sharp concentration increase at the transition-layer between suspension and bedload, whereas the deepest concentration measured in 2011 was 6.67 g/L. Successful river bed dredging in 2007 returned only gravels and pebbles, suggesting that sand was entirely in suspension. However, the available data are too scarce to unravel the exact bedload concentration.
Narayani River suspended sediments are principally composed of fine to medium sand (following the Wentworth grain size chart), and mainly display unimodal grain size distributions (supporting Fig. S9). The 2011 depth profiles display a clear downward coarsening as illustrated by the constant increase with depth of the size of the 90th percentile of the grain size distribution D90 (Fig. 5), as expected from Rouse and other suspension theories (Rouse & others, 1950; Garcia, 2008). Surprisingly, i.e., in contrast with these

suspension theories, we do not observe significant variations of the grain size gradient with depth when discharge varies between 3,000 and 7,000 m^3/s.

We explored lateral variability of $Cs(z)$ using two depth profiles sampled in sequence between 1000 and 1130 local time on 7 August 2011 with almost equal hydrological conditions. The first profile (samples #CA11125–CA11128) was realized on the axis of the river and the "off-axis" profile (samples #CA11129–CA11131) was realized at ¼ of the channel width from the right bank. The on-axis and off-axis $Cs(z)$ profiles are the same, suggesting efficient lateral diffusion of turbulence and of the sediment load over the river section. This result is coherent with the observed similarity between the surface concentrations measured at the middle of the river (Narayanghat bridge) and along the riverbank (DHM gauging station; see previous section).

The exact reasons why the concentration and grain size data display a roughly uniform gradient with depth and seem poorly dependent on the discharge are beyond the scope of this study. We rather build on the observed linear increase of concentration with depth, valid at least for discharge values between 3,000 and 7,000 m^3/s (i.e., during 70% of the monsoon period), to perform depth integration in sediment flux calculations. For that, we approximate the suspended load concentration at depth z and time t, $Cs(z,t)$, by the linear relation:

$$Cs(z,t) = (1 + K \times z) \times Cs(0,t), \quad (1)$$

where $Cs(0,t)$ is the surface concentration and $K = 0.12 \pm 0.04\ m^{-1}$ is the average slope of the Cs profiles as estimated from the depth sampling profiles. Based on the absence of significant lateral variability in the concentration profiles, we additionally assume that this relation holds over the entire river section, such that the sediment flux through the river section can be derived, by first approximation, from a single Cs_0 value.

4.2.3. Sediment flux calculation

Calculating the total suspended load flux of the Narayani River during the monsoon season requires a triple integration over the water depth, channel width, and over time. To proceed, we first modeled the topography of the river channel by considering the channel profiles sounded during ADCP cross-sections #11006, 11008, 12000, and 12001, which encompass the sediment depth sampling locations (Figs. 1 and S1). We orthogonally projected the ADCP bottom channel topography with respect to the river axis, and averaged all transects into a Synthetic transversal River Section (SRS; supporting Fig. S7A). We derived a rating curve

for this mean transversal section by computing water discharge Q through that section for any local water height H between 0 and 14 m.

To estimate the water velocity distribution in the section, we hypothesize that the law of the wall applied to the whole water column (details in Appendix A), so that:

$$Q(H) = \int_{X_{lb}(H)}^{X_{rb}(H)} \int_{0}^{z_b(x)} u_{(x,z,H)}\, dx\, dz \approx \sqrt{g} \int_{X_{lb}(H)}^{X_{rb}(H)} \int_{0}^{z_B(x)} \frac{\sqrt{S_e(H)}\sqrt{z_B(x,H)}}{k} \ln\left(\frac{30(z_B(x,H) - z)}{k_s}\right) dx\, dz \qquad (2)$$

where $u(x,z,H)$ is the water velocity at lateral position x, depth z, and height H, X_{lb} and X_{rb} represent the left and right bank abscissa, $S_e(H)$ the energy slope for water elevation H, g the gravity constant, κ the Von Karman constant taken at 0.41, $z_B(x,H)$ the local bottom depth counted from the water surface, and k_s the effective roughness height here defined by $3 \times D_{50}$ = 0.22 m from the pebble median size measured on local Narayani gravel bars (supplementary Table S2; (Mezaki & Yabiku, 1984; Attal & Lavé, 2006; Dingle et al., 2016)). In equation (2), $S_e(H)$, is assumed to be constant around 0.05% (see justification and sensitivity test in supporting information S7).

To compute the total suspended load flux, we rely on the assumptions that the surface concentration is uniform at any given time, and that the depth profile $Cs(z)$ follows a linear trend of constant slope, as described in the previous section. The instantaneous sediment flux can thus be simplified, according to equations (1) and (2), into:

$$Q_s(t) = \int_{X_{lb}(t)}^{X_{rb}(t)} \int_{0}^{z_b(t,x)} C_s(z,t).u_{(x,z,Q(t))}\, dxdz = C_{s0}(t)\left(Q(t) + K \int_{X_{lb}(t)}^{X_{rb}(t)} \int_{0}^{z_b(t,x)} z.u_{(x,z,Q(t))}\, dxdz\right). \qquad (3)$$

This double integration of z and u on space variables was numerically performed, but can be approximated for rapid use by the closely fitting relationship that we homogeneised in dimension:

$$Q_s(t) = C_{s0}(t) \times Q(t) \times (1 + K^* \times \exp(-1.9561 + 0.5517 \times \log(\frac{Q(t)}{Q^*}) - 0.0185 \times \log(\frac{Q(t)}{Q^*})^2).$$

where, $K^* = 0.12$ dimentionless and $Q^* = 1\ m^3/s$.

Finally, to realize time integration, we can follow distinct pathways. DHM discharge measurements provide an hourly record, whereas our suspended load sampling was performed on a daily basis. To compute sediment flux over the monsoon period or an entire year, we assume that the hydrology of the Narayani River is slowly varying and that the concentration measured each day at 0800 local time is representative of the mean concentration during that day. In this first case (case DMC), we simply assess the mean daily

discharge from the daily value measured at the DHM gauging station, derive the water height at the SRS from the synthetic rating curve, insert the measured surface concentration into equation (3), interpolate values between biweekly measurements during the monsoon period, and sum the daily mean sediment fluxes over the entire year.

In a second approach, we recognize that the large daily variations observed in our *Cs*(*t*) data might be related to higher frequency variations during a day. In that case, we need to define an empirical sediment rating curve. Classically, the suspended load concentration is linked to water discharge through a power law, which holds when a river system is transport limited, i.e., when available sediment on the channel bottom is unlimited and only hydrodynamic conditions determine a river's sediment carrying capacity. However, in active mountain ranges, rivers are mostly supply-limited (Fuller et al., 2003; Andermann et al., 2012a), and a plot of discharge against concentration displays poor correlation or non-linear behavior, including hysteresis (Fig. 4a).

To document sediment flux, we chose to explore three hypotheses or relations in estimating the hourly values of *Cs*(*t*) (Table 2 and supporting information S7).

One of the aims of this study was to improve former sediment flux estimates for the Narayani River, in particular by integrating C_s along the water column based on depth sampling measurements. Accounting for increasing concentration with depth, i.e., the second integral member in equation (3), increased the calculated sediment flux by ~45% compared to the constant concentration profile case (case DMC0 in Table 2). In contrast, the time integration scheme has much less impact on the results: the four calculations using different time-step integrations or concentration estimates (cases DMC and the three hourly-based calculations in supporting information S7) lead to very similar estimates ranging between 140 ± 14 and 158 ± 15 Mt/yr (Table 2). We thus estimate the annual suspended load flux in 2010 to be 151 ± 20 Mt/yr.

To document the timing of sediment delivery, cumulative fluxes were calculated over the year and are presented in Figure 6 normalized to their respective total budgets and compared to the discharge and direct runoff chronicles. Clear increases in sediment flux are observed during periods of sustained rainfall and intense runoff, regardless of the sediment flux calculation. Even if the rainy episode during Julian days 230–238 yielded 20–25% of the annual sediment budget, most of the suspended sediment volume exported by the Narayani River results from the cumulative effect over the whole monsoon rather than from a few

events. This moderate sensitivity of the total flux to extreme events (and conversely to the dominant role of cumulative average monsoonal floods) explains a priori that the four explored methods for calculating sediment flux converge toward relatively similar values.

4.2.4. Average sediment flux over recent decades

In active mountain ranges, landslides are considered as the major hillslope erosion process and thus the major source of river sediments. Because of the stochastic nature of landslides and mass wasting, and given that the erosional budget may be dominated by rare and very large landslides (Hovius et al., 1997), we consider that the annual sediment flux should also be stochastic by nature (Fuller et al., 2003) and should vary interannually. Deriving a mean erosional flux for the Narayani basin therefore requires averaging the sediment flux over several years or decades. Accounting for increasing sediment concentration with depth using equation (3), we derived sediment flux by applying the aforementioned DMC approach to the 14 noncontiguous years of available DHM sediment records and corresponding daily discharge records. We also used the HCC approach (Table 2) on a daily basis to derive direct runoff components to complement numerous gaps in the database.

The results display two basic domains: before 2000, annual sediment fluxes (Fig. 7) varied greatly, with annual fluxes up to 150% higher than our reference year 2010 and large interannual variations. In contrast, since 2000, the annual fluxes were less scattered. We partly ascribe the higher values pre-2000 to the use of integrative USGS sampling bottles during the early recording years, which implies that the concentration increase with depth was already accounted for in the raw data. We do not know, however, when the protocol changed to surface sampling. In the absence of further information, we limited our averaging period for the mean flux calculation to the years after 2000. During that period, the average suspended load flux was 135 ± 15 Mt/yr, slightly lower than in 2010.

4.3. Seasonal evolution of the suspended load characteristics

The sediment flux exported by the Narayani provides essential data on the amplitude of denudation in the basin, but does not provide information on the geographical origins or erosional processes that feed the fluvial network. In this section, we assess the monsoonal evolution of each erosional process contributing to the sediment yield with different tracers: grain size evolution is used as an indicator of mass wasting inputs into the network, carbonate

content and D/H composition are used to trace contributions from northern/glaciated versus southern/unglaciated basins, and TOC is used as an indicator of soil erosion.

4.3.1. Grain size evolution: sediment inputs from mass wasting

Generally, in-channel processes lead to grain size fining during transport, either by selective transport (e.g., Paola et al., 1992)) or pebble abrasion (e.g., Attal & Lavé, 2009). Nevertheless, sediment coarsening along a river channel has been observed in mountain ranges as a result of variations in hillslope sediment supply (e.g., Brummer & Montgomery, 2003; Attal & Lavé, 2006; Struck et al., 2015). In this study, we analyze grain size evolution during an entire year at the basin outlet to infer the evolution of the sediment supply in response to climatic forcing.

Figure 8 presents the evolution of the suspended sediment grain size distribution synthesized by D10, D50, and D90, the surface sediment concentration Cs_0, and river discharge at the Narayani basin outlet during the 2010 monsoon (see also supporting Figure S8 for the full cumulative distribution curves and Figure S9 for the time-series of the sediment fraction finer than 4.5 μm).

During the three monsoonal months, sediment sizes D10, D50, and D90 roughly follow fluctuations of Cs_0 with high-frequency variations occurring with amplitude of a factor of 2–3. The three most prominent peaks on Julian days 182, 215, and 242 are coincident with peak Cs_0 values of 4–8 g/L, suggesting that coarser-sediment events are related to pulses of sediment supply triggered by intense rainfall events (see sections 4.1.2 and 4.2.1). We interpret these pulses as resulting from the triggering and functioning of mass wasting processes and landslides, providing an important supply of coarser sediments (Attal & Lavé, 2006; Struck et al., 2015) during periods of continuous rainfall. Despite large daily variations, the suspended sediment grain size generally increases throughout the five months investigated: specifically, D10, D50, and D90 roughly double during the three monsoonal months, respectively starting at 3, 20, and 100 μm on Julian day 165 and reaching 6, 50, and 200 μm on Julian day 258. We also consider this trend to represent a progressive overwhelming of the sediment supply by coarse mass-wasting-derived materials.

During about three weeks after the monsoonal months (late September to mid-October; Julian days 270–290), D10, D50, and D90 abruptly coarsen to 20, 200, and 350 μm, respectively. Since mass wasting should have stopped providing sediments to the channels when rainstorms ceased (~Julian day 270), the drainage system acts as a semi-closed system,

essentially carrying only the available sediments that accumulated during the monsoon. In contrast to the monsoon, we interpret this postmonsoon coarsening to result from transport in channels, which induces a progressive flush of the more easily transported fine sediments and a delay in the arrival of slower coarser sediments.

4.3.2. Evolution of δD and carbonate content: N-S source tracers

Because the Narayani basin presents contrasted lithologies from north to south, the suspended sediment composition can be used to discriminate the N-S provenance of sediments exported at the basin outlet. Carbonates mostly outcrop in the western and northern part of the basin (Dhaulagiri and Annapurna Massifs) in the TSS rather than in the crystalline High Himalayan range (Colchen et al., 1986). The tributaries draining the TSS display a large range of carbonate content, up to 65%. Sands sampled along the banks of the upper Marsyandi tributaries have intermediate carbonate contents from 25 to 30% (Fig. 10 and supporting Table S) whereas suspended loads sampled in rivers draining mostly TSS units present slightly higher proportions of 40 ± 7%. Dudh khola sediments display exceptionally low carbonate contents because its drainage system is dominated by leucogranites. In the south flank, Marsyandi tributaries carry much lower proportions of carbonates, between 0 and 8%, which mostly originate from the upper LH units. In the East, the Trisuli river and its tributaries carry minute amount of carbonates as TSS is restricted to the Bothe Kosi far to the north of its basin (Galy et al. 1999). Narayani River sediments have variable carbonate contents from 5 to 25% (Fig. 9a and Table 1), with typical values between 10 and 20%. The average content (sediment-flux-weighted average) of the material delivered by the Narayani River from May to mid-October is 14.8%, implying that at least 30% of the Narayani suspended load derives from the TSS (~40% carbonates) and 70% from other geological units (0–8% carbonates).

The hydrogen isotopic composition of hydrated silicates reflects both the original bedrock composition (i.e., metamorphic water mostly contained in micas and chlorites, with δD values around –90‰ (France-Lanord & Sheppard, 1988) and water incorporated into secondary minerals as hydroxyl during weathering. The isotopic composition of the latter depends on that of local meteoric water, which in the Himalaya is dependent on the combined effects of distillation linked to orographic precipitation and elevation (Garzione et al., 2008). Consequently, river sediments derived from the northern watersheds and glaciated

environments display low δD values around –160 to –110‰, such as sediments of the upper Marsyandi, Naur, Dudh, Dona rivers, or Langtang area in the eastern part of the Narayani watershed (see location in Fig. 1), particularly the fine sediments (glacier flour) collected at the outlet of the pro-glacial streams in front of Dudh and Langtang glaciers (Fig. 10). In contrast, river sediments from lower elevations along the southern flank of the Himalaya or from tributaries draining elevated TSS lithologies along nonglaciated basins (Sabche, Bratang or Ghatte rivers in the Upper Marsyandi), display higher δD values between –100 and –80‰ (Khudi, Chepe, Darondi, Dordi, Paudi, Ngadi khola on Fig. 10), similar to pristine bedrock values. These results suggest that lower δD values are preferentially indicative of sediments issued from weathering associated with glacial erosion.

Hydrated silicates in Narayani River sediments span a wide range of δD values over the monsoon period, from –87 to –117‰ (Fig. 9), with high-frequency variations but no seasonal trend. Most days (72.5%) present a δD value greater than –100‰, consistent with a dominant signature of unweathered bedrock or weathered material issued from the southern Himalayan flank, whereas some days display isotopic compositions that require a significant or even dominant contribution of sediments issued from the upper glaciated catchments. When compared to the contribution of ice melting to the Narayani River discharge, the glacial sediment contribution is apparent during the premonsoon and early monsoon periods (Fig. 11, supporting Text S10).

Daily Narayani suspended sediment samples appear to cover almost the full spectrum of carbonate and δD compositions documented within the basin from north to south, and show a rough anti-correlation (Fig. 10). It is consistent with the fact that a large fraction of the glaciers feeding the Narayani River, mostly in the Annapurna and Dhaulagiri basins, are eroding TSS carbonate-rich formations. During the premonsoon and early monsoon periods (before Julian day 180), the δD data appear to follow the relative contribution of ice melting to the Narayani discharge, with the most negative value recorded in mid-June (Julian day 163) when ice melting had reached a maximum contribution of ~50% (Figs. 3 and 11). This overall agreement during a month-long period is only interrupted by the first major monsoonal rainfall event on Julian day 171, which produced a fivefold increase of the suspended load concentration (Fig. 3b) and probably diluted the glacial sediment signal during a couple of days. In contrast, the relative contribution of ice melting was lower than 10% during the monsoon, and no clear relation was found to explain the observed δD

variations. This lack of correlation probably reflects that glacial erosion and erosion of carbonates can be locally uncorrelated: in the eastern part of the Narayani watershed or in the Manaslu area, glaciers primarily erode granitic or gneissic massifs, whereas a large portion of the carbonate-rich TSS lithologies outcrop along unglaciated hillslopes. Both carbonate content and δD values show similar high-frequency variations, indicating that the origin of the sediments, whether related to distinct geographic sources or an erosion process, can vary quite abruptly throughout the season and rapidly respond to local events and meteorological conditions.

4.3.3. Evolution of TOC: superficial soil erosion

TOC in the top horizons of soil profiles in the Himalaya reach very high values from a few to more than 10 wt% (e.g., Lorphelin, 1985; Right & Lorphelin, 1986; Shrestha et al., 2004; Bäumler et al., 2005; Caspari et al., 2006; Dorji et al., 2009). In this study, we use TOC as an indicator of the proportion of soil-derived material in the Narayani suspended sediment.

Daily measurements of TOC in Narayani suspended sediments during 2010 varied between 0.2 and 1.3 wt%. During the premonsoon period TOC are high, around 1 wt%, and drop to 0.2–0.5 wt% after the first heavy rainfall and discharge event on Julian day 171 (Fig. 9b) and through the postmonsoon season. Organic carbon was reported to be preferentially associated with fine particles in Himalaya-derived sediments (Galy et al., 2008). During the monsoon, TOC in the Narayani suspended load follow the grain size-controlled relation established for large Himalayan rivers by Galy et al. (2008), despite large scatter (supporting Fig. S11). In contrast, during the premonsoon period, TOC values are well above the Himalayan rivers trend while fine sediment proportions are important (supporting Fig. S11). Therefore, grain size sorting in the water column cannot account for such high TOC when discharge and sediment suspension are low. Although TOC is not a completely conservative tracer because it is affected by various processes during fluvial transport (e.g., Battin et al., 2008; Galy et al., 2008), high TOC in Narayani River sediments during the premonsoon period could reflect higher inputs from sources enriched in soil or organic matter (vegetal litter). During the monsoon, Narayani TOC values remain low in the 0.2 to 0.5 wt% range. This is above the range of bedrock (0.05 to 0.1 wt%, Galy et al. 2007) but much lower than soil derived material, which we interpret as evidence that the contribution of soil erosion is dwarfed by that of mass wasting.

5. Discussion

5.1 Sediment flux calculation: depth sampling and general strategy

Previous estimates of the Narayani suspended load flux are 100 ± 50 Mt/yr (Sinha & Friend, 1994; Andermann et al., 2012a). Our estimates of 150 ± 20 Mt/yr for 2010 and 135 ± 15 Mt/yr during the previous decade based on DHM data are in the higher range of previous estimates because they account for vertical variations of concentration with depth, whereas we obtain a flux around 100 Mt/yr when this gradient is ignored (case DMC0, Table 2). Thus, even when the Narayani River is highly turbulent during monsoonal floods, vertical sorting must be integrated into the sediment flux; otherwise the Narayani sediment flux can be underestimated by up to 50%. Our approach to integrating the concentration over depth is simplified and based on measurements operated during only a few days. To perform depth integration on a more physical basis, a complementary study would be necessary to document the concentration gradient during low to intermediate (<3,000 m^3/s) and very high flows (>7,000 m^3/s). However, as the range of flow conditions during our sampling campaigns encompasses >85% of the exported sediment flux (due to reduced load flux at low flow and the rare occurrence of the highest flow conditions), we do not expect major bias in our estimates. Furthermore, the depth-integration term in equation (3) depends only on the water discharge and can be applied to any future (or past) record of surface suspended load concentration without depth sampling.

However, given the highly variable rating curves obtained from DHM data between 1975 and 2012 (supporting Fig. S12) and the geomorphologic considerations previously mentioned, we suggest that deriving a unique and constant sediment rating curve in a supply-limited system is probably not relevant (see also section 5.4). Even if sediment production and mobilization on hillslopes seem roughly correlated to runoff flow, by assuming the robust relation between direct discharge and sediment flux (supporting Fig. S7C), the relation $Qs = f_2(Qd)$ can vary amply through time. This is likely related to the stochastic behavior of very large contributing landslides, or the complex combined control of ground saturation and rainfall intensity in triggering landslides (Gabet et al., 2004b; see also section 5.3), implying that the dependency of sediment flux on direct discharge also varies through time. The 14 years of DHM sediment chronicles suggest that such variations need to be accounted for at least on an annual basis. The small clockwise hysteresis observed in the June 2010 sediment flux (supporting Fig. S7C) might suggest that such variations should be considered even on a monthly to weekly basis.

5.2 Mean denudation rates

Deriving a mean landscape denudation rate requires a good estimation of the bedload flux to complement the suspended load flux. As mentioned earlier, bedload fluxes cannot be investigated in detail because of the technical difficulties in dredging the pebble-rich bottom sediment during high floods. Based on four lines of evidence developed in supporting Text S13, we estimate the bedload flux to be less than 10 Mt/yr, which provides a mean erosion rate estimate in the Narayani basin of $1.6^{+0.35}_{-0.2}$ mm/yr over the last decade.

This rate is clearly higher than estimates obtained from the suspended load in smaller subcatchments that drain the active southern flank of the Nepal Himalayas (scattered values between 0.1 and 0.3 mm/yr and up to 2.8 mm/yr; Wulf et al., 2012), the Langtang Valley (~0.1 mm/yr; Chhetri et al., 2016), or the upper and middle Marsyandi (0.1–0.7 mm/yr, except for a small subcatchment that reaches 1.3 mm/yr; Gabet et al., 2008). Considering that sediment transfer is quasi-instantaneous at the scale of the monsoon season (see section 5.4), and that there is no dilution or buffering effect of the sediment source signature, it is not clear how to reconcile such small rates with that measured at the Narayani outlet, which must represent the sum of the sediment delivery from these subcatchments. The missing part of the puzzle could be related to undocumented subcatchments (Bhuri and Seti Rivers), much higher bedload proportions in upstream areas, or, in the case of the Marsyandi river (Gabet et al., 2008), the reduced recording duration (3–4 yr) that could have missed characteristic years of heavy monsoons and higher hillslope erosion.

In contrast, our average erosion rate computed over the last decade is in close agreement with the average denudation rate of 1.7 ± 0.2 mm/yr calculated from ^{10}Be cosmogenic dating of Narayani River sands sampled over several years at the same location (Lupker et al., 2012a). Our result thus suggests that erosion during the last decade has been representative of Late Holocene denudation obtained by cosmogenic nuclides. Yet, in the specific case of the Narayani, ^{10}Be-derived values average erosion rates over ~500 yr, i.e., over one to two seismic cycles for large (Mw ≥ 8) events (considering estimated return periods of ~200 yr (Avouac et al., 2001)). If the co-seismic landslides in the Himalaya would significantly contribute to long-term landscape erosion, our results on the last decade sediment yields would be higher than ^{10}Be-derived erosion rates. Therefore, we think that the co-seismic

landslides contribution to the long-term erosion remains minor in the Narayani basin, in contrast to other locations along the Tibetan margin (Parker et al., 2011).

In this respect, Roback et al. (2018) recently provided data that allow estimating the co-seismic landslides sediment yields. They explored the distribution and volume of co-seismic landslides associated with the last Mw 7.8 earthquake that hit central Nepal on 25 April 2015, and concluded that the total mass wasting reached 0.1 to 1 km^3 and was mostly produced above a rupture area on the Main Himalayan Thrust of ~150 × 50 km (Avouac et al., 2015). This corresponds to a co-seismic contribution to erosion of 0.07–0.66 mm/yr assuming a 200-yr return period (i.e., assuming that this earthquake was associated with an average slip value of 4 m and that long term slip rates reach ~20 mm/yr; (Lavé & Avouac, 2001)).

Compared to our last decade estimate of $1.6^{+0.35}_{-0.2}$ mm/yr, the lower range of this estimate (0.07 mm/yr) agrees with our conclusion that co-seismic landslides do not represent a significant contribution to the denudation budget. Whereas the higher range of 0.66 mm/yr would suggest that they can represent up to 40% of the budget.

In conclusion, equivalence between sediment yields over the last decade and ^{10}Be-derived erosion rates involves that only a minor fraction of the co-seismic mass-wasting material is delivered to the base of hillslopes and to colluvial channels, and is finally exported by the fluvial network. Further estimate of the co-seismic landslides sediment yields delivered to the fluvial network will bring additional constraint on whether or not they significantly contribute to the long-term landscape erosion.

5.3 Climate control and erosion contributions to Narayani sediment fluxes

Sediments transported by the Narayani River are derived from three main processes: glacier erosion, mass wasting and shallow to deep-seated landslides, and soil erosion. Deciphering the contributions of these erosion processes to the sediment flux is challenging, but our dataset provides some constraints.

5.3.1 Erosion by hillslope mass wasting and landslides

In active mountain ranges (excluding glaciated areas) the major erosion process is usually ascribed to landslides, and particularly deep-seated landslides. In the Himalaya, landslides are frequent (Fort, 1987; Shroder, 1998; Shroder & Bishop, 1998), can mobilize volumes of a

few km^3 (Weidinger, 2006), and can be a major contributor to the erosion budget (Gallo & Lavé, 2014). Deep-seated landslides are mainly triggered by monsoon precipitation (Iverson, 2000; Gabet et al., 2004b) that maintains a high pore-water pressure in the subsurface and decreases slope stability (Terzaghi, 1962; Carson, 1976; Hoek & Bray, 1977). In central Nepal, Gabet et al. (2004b) highlighted the role of daily rainfall intensity, beyond the role of pore pressure and water table elevation, in landslide activation and sediment production. The correlation between *Cs* and direct runoff (related to rainfall intensity; Fig. 5b), superficial runoff, and water saturation in the soil and regolith supports the view that sediment production is proportional to rainfall intensity (Gabet et al., 2004b). To explore this presumed double influence of groundwater pore pressure and rainfall intensity, we redraw the cumulative precipitation vs rainfall intensity plot (Gabet et al., 2004a) using instead the sediment flux amplitude as a function of baseflow and rainfall intensity (Fig. 12).

In the hydrologic and flow separation models used in this study (see also Eckhardt, 2005), baseflow is linearly related to the mean water table, such that in Figure 12 it can be considered as a reasonable proxy of the average pore pressure in the fractured rocky substrates of the watershed. This graph illustrates the double influence of rainfall intensity and water table depth in increasing the intensity of erosional events and thus sediment delivery to the river network. The link between water table depth, pore pressure, and landlide triggering suffers no physical ambiguity, and we can clearly pinpoint the signature of landslides in erosion of the Narayani basin: a minimum baseflow of 2,500 m^3/yr (~6 mm/d of equivalent runoff on Fig. 3b, attained after mid-July in 2010) seems required to trigger numerous or massive landslides and deliver sediment fluxes >20 t/s. The physical link between sediment flux and rainfall intensity is more equivocal. It could be related to hillslope erosion through a rapid increase of pore pressure either in high permeability fracture systems in the bedrock, more easily triggering deep-seated landslides, or in the soil and regolith, causing numerous shallow landslides. It might also be related to sediment transport capacity in headwater and low-order channels: only high surface-runoff events would be able to transport the sediment mobilized by landslides in upper and midvalley slopes or the sediment available in the secondary channel network. In either case, hillslope erosion by landslides seems required in the days before or during a precipitation event to provide brecciated and finer material, unprotected by vegetation cover, available for transport by overland flows. Otherwise we would observe high sediment fluxes associated with heavy rainfall events during the premonsoon and early monsoon periods, which is not the case.

Although landslides overwhelmed the other erosion signals after the monsoon onset (Julian day 182), constraining sediment generation by erosion processes other than landslides in our Narayani records would require focusing on the premonsoon and early monsoon periods, when landslides are not yet active. In the following subsections, we try to identify glacial and superficial soil erosion mostly during that period.

5.3.2 Glacial erosion

Glacial erosion can locally outpace the erosion rates in fluvial landscapes (Hallet et al., 1996). Thus, we hypothetically suppose that glacial erosion might dominate sediment delivery, or at least be apparent in the suspended load record, during the premonsoon and early monsoon periods when snow melting contributes significantly to the water discharge. According to melting models based on MODIS data of temperature and snow cover, 10–12% of the annual water discharge in the Narayani watershed is derived from ice/snowmelt (Bookhagen & Burbank, 2010; Andermann et al., 2012b). Moreover, direct measurements at Himalayan glacier outlets (Rana et al., 1996; Shea et al., 2015) indicate that water discharge associated with melting increases in early June (particularly ice melting), peaks around mid- to late July, and ceases by the end of September. Glacial erosion is thus expected to represent about 10% of the annual sediment flux (see details in supporting Text S10C).

In Himalayan glaciers, clockwise hystereses in sediment-load-discharge rating curves, described in the upper Marsyandi (Gabet et al., 2008) and further west in Garhwal Himalaya, India (Hasnain & Thayyen, 1999; Haritashya et al., 2010), have been ascribed to the progressive depletion of glacier-derived sediments during the course of the melting season. Consequently, the flux and concentration of glacier sediments generally peaks in June or July (Hasnain & Thayyen, 1999; Gabet et al., 2008). This clockwise hysteresis could be invoked to explain the hysteresis observed in the Narayani suspended-load record (Fig. 4a), although Anderman et al. (2012) showed that unglaciated catchments also present a similar hysteresis. Furthermore, the hysteresis of glacial sediments is shifted one month ahead of that of the Narayani: half of the annual sediment export is delivered by mid-July in front of glaciated areas compared to mid-August in the Narayani sediment flux. Both arguments rule out a dominant role of the glacial-sediment hysteresis further downstream, instead supporting the hypothesis of dilution of landslide-derived sediments by groundwater baseflow in the observed Narayani hysteresis (fig 4a).

In the Narayani basin, glacial sediments present a specific signature combining low δD values, potentially high carbonate content, and a high proportion of fine-grained material associated with glacial flour production (the median size of glacial flour ranges between ~5 (Fairchild et al., 1999) and ~30 μm (Thayyen et al., 1999; Haritashya et al., 2010)). Two weeks of the premonsoon period (Julian days 153–168) are characterized by relatively negative δD compositions culminating on day 163 with δD = –117‰. Those two weeks correspond to a high proportion (15–20%) of sediments finer than 4.5 μm and high carbonate proportions (above 17%) suggesting a north flank origin, where glaciated areas are more extensively developed. Additionally, this period corresponds to the largest relative contribution (~50%) of ice melting to the Narayani discharge. After mid-June, despite the continued increase of ice melting until mid-July, glacial melt waters are diluted by the increasing monsoonal rainfall flux. After 17 June (Julian day 168), δD values increase close to those representative of unweathered bedrock (–90 to –95‰), suggesting that the glacial sediment flux, although increasing until mid-July, is largely diluted in the massive supply of landslide material during the monsoon. Some lower δD values (<–110‰) were occasionally observed later during the monsoon, such as Julian day 199; that day was at the end of a one-week-long drier period characterized by reduced precipitation, direct runoff, and suspended sediment concentration. Because of the temporarily reduced monsoonal precipitation during that time, the isotopic fingerprint of glacial-derived sediments was exceptionally apparent in the Narayani suspended load. Landslide-derived materials dominated the sediment budget during the remainder of the monsoon period due to either direct production on slopes or mobilization of previously produced materials (e.g., colluvial deposits).

5.3.3 Soil erosion

Soil erosion is expected to provide fine materials rich in organic matter from the southern flanks of the Himalaya where most of the precipitation runoff occurs. During the premonsoon period, Narayani sediments are fine grained with high TOC (around 1%), in clear contrast to the monsoon period when coarser sediments have TOC values around 0.2–0.4% (Figs. 9b and 11). In detail, organic carbon exported with Narayani sediments seems to describe a mixing between two grain size-related end-members that depends on the period of sampling (supporting Fig. S11). During the monsoon, TOC values are slightly enriched compared to Himalayan bedrock organic carbon (0.05 to 0.1 wt%, Galy et al. 2007) and might partly correspond to graphitic carbon issued from metamorphic bedrock, as described in Himalayan

river sediments (Galy et al., 2008b). The grain size control on TOC in this first (monsoonal) population is relatively weak, and seems to follow the general trend identified in major Ganga tributaries and 2011 depth-profiles (dashed line and dots on Fig. S11; (Galy et al., 2008a)). In contrast, premonsoonal TOC values are two to three times higher than those of the grain size-controlled monsoonal trend. This latter observation confirms that these high TOC values are not an artefact controlled by grain size, but indicate significant addition of soil-derived material to the Narayani sediment load during the premonsoon period. The smaller grain size during that time is also compatible with a soil signature (supporting Figs. S9 and S11), although we cannot rule out alternative explanations such as low discharge and turbulence limiting the coarse grain suspension and/or glacial fine-sediment contributions (Thayyen et al., 1999).

Regardless of such possible grain size effects, the combination of high TOC and finer-grained than average sediments let us suppose that soil-derived sediments arrive in the Narayani River in sufficient proportion to be detected in the bulk sediment during the premonsoon period. To explain this premonsoonal enrichment in soil-derived material, we suppose that the first rainfall events trigger very shallow landslides or soil slides, export easily-mobilized sediments produced by human (e.g., agricultural) activities, or perhaps flush away organic litter that accumulated in low order channels or talweg bottoms during the dry season.

By late June (~Julian day 182), Narayani sediment TOC decreases to the bedrock value, then remains stable and low through the postmonsoon period (Fig. 9b). However, during that time, we cannot elucidate if easily-mobilized organic-carbon-rich materials were oxidized after being flushed away during the early monsoon, or if the soil signature is simply overwhelmed by landslide-derived material.

Estimating an exact budget of soil-rich material in the Narayani sediment flux is beyond the scope of our available data. However, considering that less than <5% of the annual sediment budget has transited the Narayani when soil erosion becomes minor in the bulk sediment (i.e., around Julian day 182), and considering that part of this flux is related to glacial sediments, we suspect that soil erosion contributes at most a few % to the Narayani erosional budget, as described in anthropogenically developed basins of the Himalayan Hills (West et al., 2015).

All the above considerations, including the sediment load response to rainfall and hydrology, the cumulative sediment flux curve (Fig. 6), and the relative stability of the TOC and δD trends at values similar to the bedrock average during the monsoon (Fig. 9), confirm that landslides represent the dominant erosion process in the central Himalaya, overwhelming glacial and soil erosion.

5.4 Dynamics of the Himalayan supply-limited geomorphic system

Our data present striking high-frequency (daily) variations in suspended load concentration, TOC, and carbonate content, indicating that the origin of the sediments, whether related to distinct geographic sources or erosional processes, varies quite abruptly throughout the season. Such rapid changes must represent the response to local events and meteorological conditions. For example, the intense rainfall event on day 171 briefly interrupted the glacial sediment imprint by a sudden rise in δD value and TOC, and a drop in carbonate content, before returning to the former tendency in only one or two days. This implies that the residence or transfer time of suspended sediments in such a wide Himalayan basin can be remarkably short.

Assuming average water velocities of 3–5 m/s in the Narayani River network during the monsoon, the transfer time of water from the headwaters of major tributaries (over distances of 200–300 km for Kali, Marsyandi, Trisuli) to Narayanghat ranges between 10 and 30 h. The transit time of water from the southern flank, which receives more precipitation, is around two times lower. These results are in good agreement with the close time correspondence between daily rainfall and direct discharge.

The high variability of the sediment export suggests that the suspended load travels almost as fast as water from the eroded hillslopes, and more importantly that there is no exchange or mixing with reworked fine sediments stored along the river network channels, such as several sand bars observed along the lower Trisuli. It seems that the volume of reworked fine sediments, or the dynamic of their re-erosion during flooding, is not sufficient to exchange in large proportions with the transported load, which would dampen the observed geochemical signatures. In other words, the Narayani fluvial network does not present any memory with regard to its silt and fine sand load. This fully demonstrates that the Narayani geomorphic system is supply-limited, and that the suspended sediment load primarily depends on sediments delivered from hillslope landslides.

Complementing that scheme, the postmonsoon period illustrates how the system responds to a shortage of hillslope sediments. As soon as the heavy monsoonal rainfall stops, the sediment concentration drops to below 0.5 g/L (Fig. 3). Concomitantly, we observe a clear grain size increase that cannot be attributed to source effects because hillslopes have stopped delivering material to the river network (Fig. 8). Most likely, this grain size increase at the

end of the monsoon corresponds to processes occurring in the river network itself. Indeed, river discharge and consequently transport capacity remain high enough to transport sediment and partially mobilize bedload on the channel bottom. At least three non-exclusive processes can be invoked to interpret this postmonsoonal grain size increase: 1) a difference in transfer velocity, where coarse sands transiting in suspension and saltation are delayed and arrive several days after finer sands that transit mostly as wash load and in suspension; 2) through reworking, sediment storages (e.g., sand bars) will become increasingly depleted in fine grains, supplying progressively coarser sediments throughout the season; and 3) the remobilization of the interstitial sandy fraction during bedload transport, which is generally much coarser than the average suspended load.

6. Conclusion

The acquisition and analysis of a new dataset on the suspended load concentration and geochemical characteristics of one of the largest Himalayan rivers at its basin outlet brings several important results and new perspectives on the dynamics of erosion in mountain chains by documenting three important issues as described by Romans et al., (2016): the sediment production and transfer in a natural system, the grain size partitioning and signal propagation in the drainage system, and the integration of particulate transfer dynamics with geochemical signals.

1 – Our depth sampling showed that even in a turbulent system like the Narayani River, a vertical gradient in concentration is still persistent; our study emphasizes the necessity of accounting for this concentration gradient when calculating sediment fluxes. Based on discrete depth samplings and daily surface samplings of the suspended load and flow characterization through ADCP measurements, we provide a new model to integrate sediment flux across a river section and over time. By putting bounds onto the bedload flux, which can hardly be measured in such a large and powerful river, we estimate the equivalent erosion rate during 2010 to be $1.8^{+0.35}_{-0.2}$ mm/yr. Finally, by integrating 15 years of sediment load records from DHM, we revised the previously proposed average erosion rate for Central Nepal with a tighter estimate of $1.6^{+0.35}_{-0.2}$ mm/yr. This is in close agreement with long-term (~ky) denudation rates of 1.7 mm/yr obtained from cosmogenic dating of Narayani River sands (Lupker et al., 2012a), suggesting that the long term Himalayan erosion budget is mostly driven by the annual impact of the monsoon. Although interannual variability in

monsoon strength or hillslope mass wasting seems to induce significant interannual variability in the sediment fluxes, sporadic and extreme mass-wasting events, like those associated with co-seismic landslides, appear to have little direct impact on the long term Himalayan erosion budget.

2 – By analyzing sediment fluxes and geochemical compositions, we propose δD, carbonate content, and TOC as tracers for glacial and soil-derived materials. We show that the contributions of glacier and soil erosion to the annual erosion budget are less than 10% and a few %, respectively. Their imprints in the Narayani suspended sediment load are only apparent during the premonsoon and early monsoon periods, before being diluted by landslide-derived materials during the monsoon.

3 – Our data confirm the inference of Gabet et al. (2004b) that sediment export and landslide triggering on Himalayan hillslopes are controlled by pore pressure and daily rainfall intensity. The control of pore pressure is related to accumulated precipitation during the monsoon and partly explains why the total sediment budget progressively increases during two and a half months rather than resulting from a few extreme heavy rainfall events. We confirm the previously proposed interpretation that monsoonal rainfall exerts a major control on sediment mobilization through the triggering of bedrocks landslides and mass wasting (Andermann et al., 2012a).

4 – Daily variations of the suspended load geochemical signature and the absence of delay between heavy rainfall episodes and sediment export (despite distances of hundreds of kilometers between the sediment sources and the Narayani basin outlet) suggest very short transfer times for the silt and medium sand loads. This implies a very reactive geomorphic system that is strongly supply-limited regarding the fine sediment fraction.

5 – The overwhelming contribution of landslide-derived material to the total sediment flux implies that, in the central Himalaya, as much as doubling the soil or glacier contribution to the sediment budget might be difficult to identify in sedimentary archives. This may explain why studies on sediment cores spanning the last glacial-interglacial transition in the Bengal fan (Lupker et al., 2013) show relatively unchanged provenances and were unable to evidence any increase in glacial erosion during the last glacial maximum or soil stripping following more arid climatic periods.

Aknowledgments:

The authors are grateful to Gaurav Kumar and Pr Sinha's team at IIT Kanpur, without whom the ADCP campaign and depth sampling would not have been possible. We thank Mikaël

Attal for sampling most rivers and MAR-XX in 2001, and Francois Métivier who provided the ADCP. We greatly thank Caroline Guillemette, former lab-manager at the stable isotopes laboratory at CRPG, Nancy, for her initial training on the analyses, and Celine Caillet from LIEC, Nancy, for helping us with laser grain size analyses. All data used in the manuscript are reported in the tables, figures, and Supporting Information. Meteorological, hydrological, and suspended load data can be obtained from the DHM (http://www.dhm.gov.np/). G.P. Morin was supported during his PhD by CNRS – Region Lorraine and ANR Calimero. We thank Christoff Andermann, three anonymous reviewers and the Editors for their constructive comments, which greatly helped to improve the quality of the manuscript.

References

Andermann, C., Bonnet, S., & Gloaguen, R. (2011). Evaluation of precipitation data sets along the Himalayan front. Geochemistry Geophysics Geosystems, 12(7), Q07023. https://doi.org/10.1029/2011GC003513

Andermann, Christoff, Crave, A., Gloaguen, R., Davy, P., & Bonnet, S. (2012a). Connecting source and transport: Suspended sediments in the Nepal Himalayas. Earth and Planetary Science Letters, 351–352, 158–170. https://doi.org/10.1016/j.epsl.2012.06.059

Andermann, Christoff, Longuevergne, L., Bonnet, S., Crave, A., Davy, P., & Gloaguen, R. (2012b). Impact of transient groundwater storage on the discharge of Himalayan rivers. Nature Geoscience, 5(2), 127–132. https://doi.org/10.1038/ngeo1356

Anders, A. M. A., Roe, G. H. G., Montgomery, D. R., & Finnegan, N. J. (2006). Spatial patterns of precipitation and topography in the Himalaya. Geological Society of America Special Paper, 398(03), 39–53. https://doi.org/10.1130/2006.2398(03)

Armitage, J. J., Duller, R. A., Whittaker, A. C., & Allen, P. A. (2011). Transformation of tectonic and climatic signals from source to sedimentary archive. Nature Geoscience, 4(2), 1–5.

Arnold, J. G., & Allen, P. M. (1999). Automatic methods for estimating baseflow ad groundwater recharge from streamflow records. Journal of the American Water Resources Association, 35(2), 411–424. https://doi.org/10.1111/j.1752-1688.1999.tb03599.x

Arnold, J. G., Allen, P. M., Muttiah, R., & Bernhardt, G. (1995). Automated Base Flow Separation and Recession Analysis Techniques. Ground Water, 33(6), 1010–1018. https://doi.org/10.1111/j.1745-6584.1995.tb00046.x

Attal, M, & Lavé, J. (2006). Changes of bedload characteristics along the Marsyandi River (central Nepal): Implications for understanding hillslope sediment supply, sediment load evolution along. Tectonics, Climate, and Landscape Evolution, 2398(09), 143–171. https://doi.org/10.1130/2006.2398(09).

Attal, Mikaël, & Lavé, J. (2009). Pebble abrasion during fluvial transport: Experimental results and implications for the evolution of the sediment load along rivers. Journal of Geophysical Research, 114(F4). Retrieved from http://www.agu.org/pubs/crossref/2009/2009JF001328.shtml papers2://publication/doi/10.1029/2009JF001328

Avouac, J.-P. (2003). MOUNTAIN BUILDING, EROSION, AND THE SEISMIC CYCLE IN THE NEPAL HIMALAYA. In Advances in Geophysics (Vol. 46, pp. 1–80). Elsevier. Retrieved from http://linkinghub.elsevier.com/retrieve/pii/S0065268703460019

Avouac, J.-P., Bollinger, L., Lavé, J., Cattin, R., & Flouzat, M. (2001). Le cycle sismique en Himalaya. Comptes Rendus de l'Académie Des Sciences-Series IIA-Earth and Planetary Science, 333(9), 513–529.

Avouac, J.-P., Meng, L., Wei, S., Wang, T., & Ampuero, J.-P. (2015). Lower edge of locked Main Himalayan Thrust unzipped by the 2015 Gorkha earthquake. Nature Geoscience, 8(9), 708–711. https://doi.org/10.1038/ngeo2518

Battin, T. J., Kaplan, L. A., Findlay, S., Hopkinson, C. S., Marti, E., Packman, A. I., et al. (2008). Biophysical controls on organic carbon fluxes in fluvial networks. Nature Geoscience, 1(2), 95–100. https://doi.org/10.1038/ngeo101

Bauer, K. K., & Vennemann, T. W. (2014). Analytical methods for the measurement of hydrogen isotope composition and water content in clay minerals by TC/EA. Chemical Geology, 363, 229–240. https://doi.org/10.1016/j.chemgeo.2013.10.039

Bäumler, R., Caspari, T., Totsche, K. U., Dorji, T., Norbu, C., & Baillie, I. C. (2005). Andic properties in soils developed from nonvolcanic materials in Central Bhutan. Journal of

Plant Nutrition and Soil Science, 168(5), 703–713. https://doi.org/10.1002/jpln.200521793

Blöthe, J. H., & Korup, O. (2013). Millennial lag times in the Himalayan sediment routing system. Earth and Planetary Science Letters, 382, 38–46. https://doi.org/10.1016/j.epsl.2013.08.044

Bookhagen, B., & Burbank, D. W. (2006). Topography, relief, and TRMM-derived rainfall variations along the Himalaya. Geophysical Research Letters, 33(8). https://doi.org/10.1029/2006GL026037

Bookhagen, B., & Burbank, D. W. (2010). Toward a complete Himalayan hydrological budget: Spatiotemporal distribution of snowmelt and rainfall and their impact on river discharge. Journal of Geophysical Research, 115(F3), F03019. https://doi.org/10.1029/2009JF001426

Bookhagen, B., Thiede, R. C., Strecker, M. R., & Box, P. O. (2005). Late Quaternary intensified monsoon phases control landscape evolution in the northwest Himalaya. Geology, 33(2), 149.

Boos, W. R., & Kuang, Z. (2010). Dominant control of the South Asian monsoon by orographic insulation versus plateau heating. Nature, 463(7278), 218–222.

Brummer, C. J., & Montgomery, D. R. (2003). Downstream coarsening in headwater channels: DOWNSTREAM COARSENING. Water Resources Research, 39(10). https://doi.org/10.1029/2003WR001981

Burbank, D. W., Blythe, A. E., Putkonen, J., Pratt-Sitaula, B., Gabet, E., Oskin, M., et al. (2003). Decoupling of erosion and precipitation in the Himalayas. Nature, 426(6967), 652–655. https://doi.org/10.1038/nature02187

Carson, M. A. (1976). Mass-wasting, slope development and climate. Geomorphology and Climate: New York, John Wiley and Sons, 101–136.

Caspari, T., Bäumler, R., Norbu, C., Tshering, K., & Baillie, I. (2006). Geochemical investigation of soils developed in different lithologies in Bhutan, Eastern Himalayas. Geoderma, 136(1–2), 436–458. https://doi.org/10.1016/j.geoderma.2006.04.017

Castelltort, S., & Van Den Driessche, J. (2003). How plausible are high-frequency sediment supply-driven cycles in the stratigraphic record? Sedimentary Geology, 157(1–2), 3–13.

Champagnac, J.-D., Molnar, P., Sue, C., & Herman, F. (2012). Tectonics, climate, and mountain topography. Journal of Geophysical Research, 117(B2). https://doi.org/10.1029/2011JB008348

Chapman, TG, Maxwell, A., & others. (1996). Baseflow separation-comparison of numerical methods with tracer experiments. In Hydrology and Water Resources Symposium 1996: Water and the Environment; Preprints of Papers (p. 539). Institution of Engineers, Australia.

Chapman, Tom. (1999). A comparison of algorithms for stream flow recession and baseflow separation. Hydrological Processes, 13(5), 701–714. https://doi.org/10.1002/(SICI)1099-1085(19990415)13:5<701::AID-HYP774>3.0.CO;2-2

Chhetri, A., Kayastha, R. B., & Shrestha, A. (2016). Assessment of Sediment Load of Langtang River in Rasuwa District, Nepal. Journal of Water Resource and Protection, 08(01), 84–92. https://doi.org/10.4236/jwarp.2016.81007

Clift, P. D., Giosan, L., Blusztajn, J., Campbell, I. H., Allen, C., Pringle, M., et al. (2008). Holocene erosion of the Lesser Himalaya triggered by intensified summer monsoon. Geology, 36(1), 79.

Coulthard, T. J., & Van de Wiel, M. J. (2013). Climate, tectonics or morphology: what signals can we see in drainage basin sediment yields? Earth Surface Dynamics, 1(1), 13–27. https://doi.org/10.5194/esurf-1-13-2013

Covault, J. A., Romans, B. W., Fildani, A., McGann, M., & Graham, S. A. (2010). Rapid Climatic Signal Propagation from Source to Sink in a Southern California Sediment - Routing System. The Journal of Geology, 118(3), 247 - 259. https://doi.org/10.1086/651539

D'Acqui, L. P., Churchman, G. J., Janik, L. J., Ristori, G. G., & Weissmann, D. A. (1999). Effect of organic matter removal by low-temperature ashing on dispersion of undisturbed aggregates from a tropical crusting soil. Geoderma, 93(3–4), 311–324. https://doi.org/10.1016/S0016-7061(99)00073-7

Dadson, S. J., Hovius, N., Chen, H., Dade, W. B., Lin, J.-C., Hsu, M.-L., et al. (2004). Earthquake-triggered increase in sediment delivery from an active mountain belt. Geology, 32(8), 733. https://doi.org/10.1130/G20639.1

Dahal, R. K., & Hasegawa, S. (2008). Representative rainfall thresholds for landslides in the Nepal Himalaya. Geomorphology, 100(3), 429–443.

Deal, E., Favre, A.-C., & Braun, J. (2017). Rainfall variability in the Himalayan orogen and its relevance to erosion processes. Water Resources Research, 53(5), 4004–4021. https://doi.org/10.1002/2016WR020030

DHM. (2003). Suspended Sediment Concentration Records. Kathmandu, Nepal: Department of Hydrology and Meteorology, His Majesty's Government.

DHM/FFS. (2004). Hydrological Data (2002–2003). Kathmandu, Nepal: Department of Hydrologyand Meteorology, Flood Forecasting Section.

Dingle, E. H., Sinclair, H. D., Attal, M., Milodowski, D. T., & Singh, V. (2016). Subsidence control on river morphology and grain size in the Ganga Plain. American Journal of Science, 316(8), 778–812. https://doi.org/10.2475/08.2016.03

Dingle, Elizabeth H., Attal, M., & Sinclair, H. D. (2017). Abrasion-set limits on Himalayan gravel flux. Nature, 544(7651), 471–474. https://doi.org/10.1038/nature22039

Dorji, T., Caspari, T., Bäumler, R., Veldkamp, a., Jongmans, a., Tshering, K., et al. (2009). Soil development on Late Quaternary river terraces in a high montane valley in Bhutan, Eastern Himalayas. Catena, 78(1), 48–59. https://doi.org/10.1016/j.catena.2009.02.018

Dubille, M., & Lavé, J. (2015). Rapid grain size coarsening at sandstone/conglomerate transition: similar expression in Himalayan modern rivers and Pliocene molasse deposits. Basin Research, 27(1), 26–42. https://doi.org/10.1111/bre.12071

Eckhardt, K. (2005). How to construct recursive digital filters for baseflow separation. Hydrological Processes, 19(2), 507–515. https://doi.org/10.1002/hyp.5675

Eckhardt, K. (2008). A comparison of baseflow indices, which were calculated with seven different baseflow separation methods. Journal of Hydrology, 352(1–2), 168–173. https://doi.org/10.1016/j.jhydrol.2008.01.005

Edwards, T. K., & Glysson, G. D. (1999). Field methods for measurement of fluvial sediment. US Geological Survey; Information Services,.

Fairchild, I. J., Killawee, J. A., Hubbard, B., & Dreybrodt, W. (1999). Interactions of calcareous suspended sediment with glacial meltwater: a field test of dissolution behaviour. Chemical Geology, 155(3), 243–263.

Filizola, N., & Guyot, J. L. (2004). The use of Doppler technology for suspended sediment discharge determination in the River Amazon / L'utilisation des techniques Doppler pour la détermination du transport solide de l'Amazone. Hydrological Sciences Journal, 49(1), 143–153. https://doi.org/10.1623/hysj.49.1.143.53990

Fort, M. (1987). Sporadic morphogenesis in a continental subduction setting: an example from the Annapurna Range, Nepal Himalaya. Zeitschrift Für Geomorphologie, 63(9), 36.

France-Lanord, C., & Sheppard, S. M. F. (1988). Hydrogen and oxygen isotope variations in the High Himalaya peraluminous Manaslu leucogranite: evidence for heterogeneous

sedimentary source. Geochimica et Cosmochimica Acta. Retrieved from http://linkinghub.elsevier.com/retrieve/pii/001670378890107X

Fuchs, M. C., Gloaguen, R., Merchel, S., Pohl, E., Sulaymonova, V. A., Andermann, C., & Rugel, G. (2015). Millennial erosion rates across the Pamir based on 10Be concentrations in fluvial sediments: dominance of topographic over climatic factors. Earth Surface Dynamics Discussions, 3(1), 83–128. https://doi.org/10.5194/esurfd-3-83-2015

Fukushima, Y., Kawashima, K., Suzuki, M., Ohta, T., Motoyama, H., Kubota, H., et al. (1987). Runoff characteristics in three glacier-covered watersheds of Langtang Valley, Nepal Himalayas. Bulletin of Glacier Research, (5), 11–18.

Fuller, C. W., Willett, S. D., Hovius, N., & Slingerland, R. (2003). Erosion Rates for Taiwan Mountain Basins: New Determinations from Suspended Sediment Records and a Stochastic Model of Their Temporal Variation. The Journal of Geology, 111(1), 71–87. https://doi.org/10.1086/344665

Furey, P. R., & Gupta, V. K. (2001). A physically based filter for separating base flow from streamflow time series. Water Resources Research, 37(11), 2709–2722. https://doi.org/10.1029/2001WR000243

Gabet, Emmanuel J., Pratt-Sitaula, B. a., & Burbank, D. W. (2004a). Climatic controls on hillslope angle and relief in the Himalayas. Geology, 32(7), 629. https://doi.org/10.1130/G20641.1

Gabet, Emmanuel J., Burbank, D. W., & Putkonen, J. (2004b). Rainfall thresholds for landsliding in the Himalayas of Nepal. Geomorphology, 63(3–4), 131–143.

Gabet, E., Burbank, D., Prattsitaula, B., Putkonen, J., & Bookhagen, B. (2008). Modern erosion rates in the High Himalayas of Nepal. Earth and Planetary Science Letters, 267(3–4), 482–494. https://doi.org/10.1016/j.epsl.2007.11.059

Gabet, E J, & Mudd, S. M. (2009). A theoretical model coupling chemical weathering rates with denudation rates. Geology, 37(2), 151–154.

Gallo, F., & Lavé, J. (2014). Evolution of a large landslide in the High Himalaya of central Nepal during the last half-century. Geomorphology, 223, 20–32. https://doi.org/10.1016/j.geomorph.2014.06.021

Galy, A. (1999, January 11). Etude géochimique de l'érosion actuelle de la chaîne himalayenne. Institut national polytechnique de Lorraine, Vandoeuvre-lès-Nancy, FRANCE.

Galy, A., & France-Lanord, C. (1999). Weathering processes in the Ganges–Brahmaputra basin and the riverine alkalinity budget. Chemical Geology. Retrieved from http://linkinghub.elsevier.com/retrieve/pii/S0009254199000339 http://www.sciencedirect.com/science/article/pii/S0009254199000339

Galy, V., Bouchez, J., & France-Lanord, C. (2007). Determination of Total Organic Carbon Content and δ 13 C in Carbonate-Rich Detrital Sediments. Geostandards and Geoanalytical Research, 31(3), 199–207. https://doi.org/10.1111/j.1751-908X.2007.00864.x

Galy, V., France-Lanord, C., & Lartiges, B. (2008). Loading and fate of particulate organic carbon from the Himalaya to the Ganga–Brahmaputra delta. Geochimica et Cosmochimica Acta, 72(7), 1767–1787. https://doi.org/10.1016/j.gca.2008.01.027

Galy, V., Beyssac, O., France-Lanord, C., & Eglinton, T. (2008b). Recycling of graphite during Himalayan erosion: a geological stabilization of carbon in the crust. *Science (New York, N.Y.), 322*(5903), 943–5. https://doi.org/10.1126/science.1161408

Garcia, M. H. (Ed.). (2008). Sedimentation transport and morphodynamics. In Sedimentation Engineering: Processes, Measurements, Modeling, and Practice. (Vol. 110, pp. 21–164). Reston, Va: American Society of Civil Engineering.

Garzione, C. N., Hoke, G. D., Libarkin, J. C., Withers, S., MacFadden, B., Eiler, J., et al. (2008). Rise of the Andes. Science (New York, N.Y.), 320(5881), 1304–7. https://doi.org/10.1126/science.1148615

Godard, V., Burbank, D. W., Bourles, D. L., Bookhagen, B., Braucher, R., Fisher, G. B., & Bourlès, D. L. (2012). Impact of glacial erosion on 10 Be concentrations in fluvial sediments of the Marsyandi catchment, central Nepal. Journal of Geophysical Research, 117(F3), 1–17. https://doi.org/10.1029/2011JF002230

Godard, V., Bourles, D. L., Spinabella, F., Burbank, D. W., Bookhagen, B., Fisher, G. B., et al. (2014). Dominance of tectonics over climate in Himalayan denudation. Geology, (January). https://doi.org/10.1130/G35342.1

Gurung, J., Ishiga, H., & Khadka, M. (2005). Geological and geochemical examination of arsenic contamination in groundwater in the Holocene Terai Basin, Nepal. Environmental Geology, 49(1), 98–113. https://doi.org/10.1007/s00254-005-0063-6

Hallet, B., Hunter, L., & Bogen, J. (1996). Rates of erosion and sediment evacuation by glaciers: A review of field data and their implications. Global and Planetary Change, 12(1–4), 213–235.

Haritashya, U. K., Kumar, A., & Singh, P. (2010). Particle size characteristics of suspended sediment transported in meltwater from the Gangotri Glacier, central Himalaya — An indicator of subglacial sediment evacuation. Geomorphology, 122(1–2), 140–152.

Hasnain, S. I., & Thayyen, R. J. (1999). Discharge and suspended-sediment concentration of meltwaters, draining from the Dokriani glacier, Garhwal Himalaya, India. Journal of Hydrology, 218(3–4), 191–198. https://doi.org/10.1016/S0022-1694(99)00033-5

Heimsath, A. M., DiBiase, R. A., & Whipple, K. X. (2012). Soil production limits and the transition to bedrock-dominated landscapes. Nature Geoscience, 5(3), 210–214.

Hodges, K. V. (2000). Tectonics of the Himalaya and southern Tibet from two perspectives. Geological Society of America Bulletin, 112(3), 324–350.

Hoek, E., & Bray, J. (1977). Rock Slope Engineering, 2nd. Edn., The Institute of Mining and Metallurgy, London, 527.

Hovius, N., Stark, C. P., & Allen, P. A. (1997). Sediment flux from a mountain belt derived by landslide mapping. Geology, 25(3), 231. https://doi.org/10.1130/0091-7613(1997)025<0231:SFFAMB>2.3.CO;2

Immerzeel, W. W., Droogers, P., De Jong, S., & Bierkens, M. (2009). Large-scale monitoring of snow cover and runoff simulation in Himalayan river basins using remote sensing. Remote Sensing of Environment, 113(1), 40–49.

Iverson, R. M. (2000). Landslide triggering by rain infiltration. Water Resources Research, 36(7), 1897–1910. https://doi.org/10.1029/2000WR900090

Iwata, S., Sharma, T., & Yamanaka, H. (1984). A preliminary report on geomorphology of central Nepal and Himalayan uplift. J. Nepal Geol. Soc, 4, 141–149.

Jerolmack, D. J., & Paola, C. (2010). Shredding of environmental signals by sediment transport. Geophysical Research Letters, 37(19), n/a-n/a. https://doi.org/10.1029/2010GL044638

Kayastha, R., Ageta, Y., & Nakawo, M. (2000). Positive degree-day factors for ablation on glaciers in the Nepalese Himalayas: case study on Glacier AX010 in Shorong Himal, Nepal. Bulletin of Glaciological Research, 17, 1–10.

Larsen, I. J., Almond, P. C., Eger, A., Stone, J. O., Montgomery, D. R., & Malcolm, B. (2014). Rapid Soil Production and Weathering in the Western Alps, New Zealand. Science (New York, N.Y.), 637. https://doi.org/10.1126/science.1244908

Lavé, J., & Avouac, J. P. (2001). Fluvial incision and tectonic uplift across the Himalayas of central Nepal. Journal of Geophysical Research, 106(B11), 26561. https://doi.org/10.1029/2001JB000359

Lebeau, O., Busigny, V., Chaduteau, C., & Ader, M. (2014). Organic matter removal for the analysis of carbon and oxygen isotope compositions of siderite. Chemical Geology, 372, 54–61. https://doi.org/10.1016/j.chemgeo.2014.02.020

Lorphelin, L. (1985). Etude d'une séquence altitudinale de sols le long d'un versant-type de l'Himalaya népalais : les sols du versant Salmé = Study of an altitudinal soils sequences along a type basin of Nepal Himalaya: the soils of Salmé basin. Université de Poitiers. Retrieved from http://cat.inist.fr/?aModele=afficheN&cpsidt=7992202

Lupker, M., France-Lanord, C., Lavé, J., Bouchez, J., Galy, V., Métivier, F., et al. (2011). A Rouse-based method to integrate the chemical composition of river sediments: Application to the Ganga basin. Journal of Geophysical Research, 116(F4), F04012. https://doi.org/10.1029/2010JF001947

Lupker, M., Blard, P.-H., Lavé, J., France-Lanord, C., Leanni, L., Puchol, N., et al. (2012a). 10Be-derived Himalayan denudation rates and sediment budgets in the Ganga basin. Earth and Planetary Science Letters, 333–334(C), 146–156.

Lupker, M., France-Lanord, C., Galy, V., Lavé, J., Gaillardet, J., Gajurel, A. P., et al. (2012b). Predominant floodplain over mountain weathering of Himalayan sediments (Ganga basin). Geochimica et Cosmochimica Acta, 84, 410–432. https://doi.org/10.1016/j.gca.2012.02.001

Lupker, M., France-Lanord, C., Galy, V., Lavé, J., & Kudrass, H. (2013). Increasing chemical weathering in the Himalayan system since the Last Glacial Maximum. Earth and Planetary Science Letters, 365, 243–252. https://doi.org/10.1016/j.epsl.2013.01.038

Meunier, P., Hovius, N., & Haines, J. A. (2008). Topographic site effects and the location of earthquake induced landslides. Earth and Planetary Science Letters, 275(3–4), 221–232. https://doi.org/10.1016/j.epsl.2008.07.020

Meyer-Peter, E., & Müller, R. (1948). Formulas for bed-load transport. In IAHSR 2nd meeting, Stockholm, appendix 2. IAHR.

Mezaki, S., & Yabiku, M. (1984). Channel geomorphology of the Kali gandaki and the Narayani rivers in central Nepal. J. Nepal Geol. Soc, 4(Special), 161–176.

Miller, R. N., Yarzab, R. F., & Given, P. H. (1979). Determination of the mineral-matter contents of coals by low-temperature ashing. Fuel, 58(1), 4–10. https://doi.org/10.1016/0016-2361(79)90044-9

Mohindra, R., Parkash, B., & Prasad, J. (1992). Historical geomorphology and pedology of the Gandak Megafan, Middle Gangetic Plains, India. Earth Surface Processes and Landforms, 17(7), 643–662. https://doi.org/10.1002/esp.3290170702

Molnar, P., Boos, W. R., & Battisti, D. S. (2010). Orographic Controls on Climate and Paleoclimate of Asia: Thermal and Mechanical Roles for the Tibetan Plateau. Annual Review of Earth and Planetary Sciences, 38(1), 77–102. https://doi.org/10.1146/annurev-earth-040809-152456

Najman, Y. (2005). The detrital record of orogenesis: A review of approaches and techniques used in the Himalayan sedimentary basins. Earth-Science Reviews. https://doi.org/10.1016/j.earscirev.2005.04.004

Nepal, S., Krause, P., Flügel, W.-A., Fink, M., & Fischer, C. (2014). Understanding the hydrological system dynamics of a glaciated alpine catchment in the Himalayan region using the J2000 hydrological model. Hydrological Processes, 28(3), 1329–1344.

Paola, C., Parker, G., Seal, R., Sinha, S. K., Southard, J. B., & Wilcock, P. R. (1992). Downstream Fining by Selective Deposition in a Laboratory Flume. Science, 258(5089), 1757–1760. https://doi.org/10.1126/science.258.5089.1757

Parker, R. N., Hancox, G. T., Petley, D. N., Massey, C. I., Densmore, A. L., & Rosser, N. J. (2015). Spatial distributions of earthquake-induced landslides and hillslope

preconditioning in northwest South Island, New Zealand. Earth Surface Dynamics Discussions, 3(1), 1–52. https://doi.org/10.5194/esurfd-3-1-2015

Parker, Robert N., Densmore, A. L., Rosser, N. J., de Michele, M., Li, Y., Huang, R., et al. (2011). Mass wasting triggered by the 2008 Wenchuan earthquake is greater than orogenic growth. Nature Geoscience, 4(7), 449–452. https://doi.org/10.1038/ngeo1154

Pike, S., Dewison, M., & Spears, D. (1989). Sources of error in low temperature plasma ashing procedures for quantitative mineral analysis of coal ash. Fuel, 68(5), 664–668. https://doi.org/10.1016/0016-2361(89)90170-1

Pratt-Sitaula, B., Garde, M., Burbank, D. W., Oskin, M., Heimsath, A., & Gabet, E. (2007). Bedload-to-suspended load ratio and rapid bedrock incision from Himalayan landslide-dam lake record. Quaternary Research, 68(1), 111–120. https://doi.org/10.1016/j.yqres.2007.03.005

Putkonen, J. (2004). Continuous snow and rain data at 500 to 4400 m altitude near Annapurna, Nepal, 1999-2001. Arctic, Antarctic, and Alpine Research. Retrieved from http://instaar.metapress.com/index/q26412408r271768.pdf
papers2://publication/uuid/B1D48630-41E7-436B-99F4-948A9E46DAC0

Racoviteanu, A. E., Armstrong, R., & Williams, M. W. (2013). Evaluation of an ice ablation model to estimate the contribution of melting glacier ice to annual discharge in the Nepal Himalaya. Water Resources Research, 49(9), 5117–5133.

Rana, B., Fukushima, Y., Ageta, Y., & Nakawo, M. (1996). Runoff modeling of a river basin with a debris-covered glacier in Langtang Valley, Nepal Himalaya. Bulletin of Glacier Research, (14), 1–6.

RD Instruments, T. (2014). WinRiver II; software user's guide. RD Instruments. San Diego, USA.

Right, D., & Lorphelin, L. (1986). Weathering of silt and clay in soils of a toposequence in the Himalayas, Nepal. Geoderma, 39(2), 141–155. https://doi.org/10.1016/0016-7061(86)90072-8

Roback, K., Clark, M. K., West, A. J., Zekkos, D., Li, G., Gallen, S. F., et al. (2018). The size, distribution, and mobility of landslides caused by the 2015 M w 7.8 Gorkha earthquake, Nepal. Geomorphology, 301, 121–138. https://doi.org/10.1016/j.geomorph.2017.01.030

Romans, B. W., Castelltort, S., Covault, J. A., Fildani, A., & Walsh, J. P. (2016). Environmental signal propagation in sedimentary systems across timescales. Earth-Science Reviews, 153, 7–29. https://doi.org/10.1016/j.earscirev.2015.07.012

Rouse, H., & others. (1950). Engineering hydraulics. In Hydraulics Conference 1949: Iowa Institute of Hydraulic Research). Wiley.

Sharp, Z., & Atudorei, V. (2001). A rapid method for determination of hydrogen and oxygen isotope ratios from water and hydrous minerals. Chemical Geology.

Shea, J., Immerzeel, W., Wagnon, P., Vincent, C., & Bajracharya, S. (2015). Modelling glacier change in the Everest region, Nepal Himalaya. The Cryosphere, 9(3), 1105–1128.

Sheppard, S. M. F., & Schwarcz, H. P. (1970). Fractionation of carbon and oxygen isotopes and magnesium between coexisting metamorphic calcite and dolomite. Contributions to Mineralogy and Petrology, 26(3), 161–198. https://doi.org/10.1007/BF00373200

Scherler, D., Bookhagen, B., & Strecker, M. R. (2011). Hillslope-glacier coupling: The interplay of topography and glacial dynamics in High Asia. Journal of Geophysical Research: Earth Surface (2003–2012), 116(F2).

Shrestha, B. M., Sitaula, B. K., Singh, B. R., & Bajracharya, R. M. (2004). Soil organic carbon stocks in soil aggregates under different land use systems in Nepal. Nutrient Cycling in Agroecosystems, 70(2), 201–213. https://doi.org/10.1023/B:FRES.0000048472.25373.7e

Shroder, J. F. (1998). Slope failure and denudation in the western Himalaya. Geomorphology, 26(1–3), 81–105. https://doi.org/10.1016/S0169-555X(98)00052-X

Shroder, J. F., & Bishop, M. P. (1998). Mass movement in the Himalaya: new insights and research directions. Geomorphology, 26(1–3), 13–35. https://doi.org/10.1016/S0169-555X(98)00049-X

Sime, L. C., Ferguson, R. I., & Church, M. (2007). Estimating shear stress from moving boat acoustic Doppler velocity measurements in a large gravel bed river. Water Resources Research, 43(3). Retrieved from http://www.agu.org/pubs/crossref/2007/2006WR005069.shtml papers2://publication/doi/10.1029/2006WR005069

Singh, S. K., Rai, S. K., & Krishnaswami, S. (2008). Sr and Nd isotopes in river sediments from the Ganga Basin: Sediment provenance and spatial variability in physical erosion. Journal of Geophysical Research, 113(F3). Retrieved from http://www.agu.org/pubs/crossref/2008/2007JF000909.shtml papers2://publication/doi/10.1029/2007JF000909

Sinha, R., & Friend, P. F. (1994). River systems and their sediment flux, Indo-Gangetic plains, Northern Bihar, India. Sedimentology, 41(4), 825–845. https://doi.org/10.1111/j.1365-3091.1994.tb01426.x

Struck, M., Andermann, C., Hovius, N., Korup, O., Turowski, J. M., Bista, R., et al. (2015). Monsoonal hillslope processes determine grain size-specific suspended sediment fluxes in a trans-Himalayan river: Mass wasting determines sediment caliber. Geophysical Research Letters, 42(7), 2302–2308. https://doi.org/10.1002/2015GL063360

Terzaghi, K. (1962). Stability of steep slopes on hard unweathered rock. Geotechnique, 12(4), 251–270.

Thayyen, R. J., Gergan, J. T., & Dobhal, D. P. (1999). Particle size characteristics of suspended sediments and subglacial hydrology of Dokriani Glacier, Garhwal Himalaya, India. Hydrological Sciences Journal, 44(1), 47–61. https://doi.org/10.1080/02626669909492202

Thomson, S. N., Brandon, M. T., Tomkin, J. H., Reiners, P. W., Vásquez, C., & Wilson, N. J. (2010). Glaciation as a destructive and constructive control on mountain building. Nature, 467(7313), 313–317.

Tolorza, V., Carretier, S., Andermann, C., Ortega-Culaciati, F., Pinto, L., & Mardones, M. (2014). Contrasting mountain and piedmont dynamics of sediment discharge associated with groundwater storage variation in the Biobío River. Journal of Geophysical Research: Earth Surface, 119(12), 2730–2753. https://doi.org/10.1002/2014JF003105

Turowski, J. M., Rickenmann, D., & Dadson, S. J. (2010). The partitioning of the total sediment load of a river into suspended load and bedload: a review of empirical data: The partitioning of sediment load. Sedimentology, 57(4), 1126–1146. https://doi.org/10.1111/j.1365-3091.2009.01140.x

Wagnon, P., Linda, A., Arnaud, Y., Kumar, R., Sharma, P., Vincent, C., et al. (2007). Four years of mass balance on Chhota Shigri Glacier, Himachal Pradesh, India, a new benchmark glacier in the western Himalaya. Journal of Glaciology, 53(183), 603–611.

Weidinger, J. T. (2006). Predesign, failure and displacement mechanisms of large rockslides in the Annapurna Himalayas, Nepal. Engineering Geology, 83(1), 201–216.

West, A. J., Arnold, M., AumaÎtre, G., Bourlès, D. L., Keddadouche, K., Bickle, M., & Ojha, T. (2015). High natural erosion rates are the backdrop for present-day soil erosion in the agricultural Middle Hills of Nepal. Earth Surface Dynamics, 3(3), 363–387. https://doi.org/10.5194/esurf-3-363-2015

Wilcock, P. R. (1996). Estimating Local Bed Shear Stress from Velocity Observations. Water Resources Research, 32(11), 3361–3366. https://doi.org/10.1029/96WR02277

Wittenberg, H., & Sivapalan, M. (1999). Watershed groundwater balance estimation using streamflow recession analysis and baseflow separation. Journal of Hydrology, 219(1–2), 20–33. https://doi.org/10.1016/S0022-1694(99)00040-2

Wolman, M. G., & Miller, J. P. (1960). Magnitude and Frequency of Forces in Geomorphic Processes. The Journal of Geology, 68(1), 54–74. https://doi.org/10.1086/626637

Wulf, H., Bookhagen, B., & Scherler, D. (2012). Climatic and geologic controls on suspended sediment flux in the Sutlej River Valley, western Himalaya. Hydrology and Earth System Sciences, 16(7), 2193–2217. https://doi.org/10.5194/hess-16-2193-2012

Yin, A. (2006). Cenozoic tectonic evolution of the Himalayan orogen as constrained by along-strike variation of structural geometry, exhumation history, and foreland sedimentation. Earth-Science Reviews, 76(1–2), 1–131. https://doi.org/10.1016/j.earscirev.2005.05.004

Table 1: Concentration (*Cs*), chemical composition, and grain size characteristics of the Narayani suspended load (SL) sampled at the surface and during vertical profiles at the Narayani basin outlet, Narayanghat. Numbers following SL in the 'type' column specify the depth of sampling for depth profiles.

Sample #	Type	Cs [g/L]	Julian day	Date [DD/MM/YYYY]	TOC [%]	δ^{13}Corg [‰]	H_2O+ [%]	δD [‰]	Carb. Cont. [%]	δ^{13}C Carb. [vPDB]	δ^{18}O Carb. [vSMOW]	Calc. Cont. [%]	Dol. Cont. [%]	δ^{13}C. Calc [vPDB]	δ^{13}C Dol [vPDB]	δ^{18}O Calc [vSMOW]	δ^{18}O Dol [vSMOW]	<4.5 µm [%]	D10 (µm)	D16 (µm)	D50 (µm)	D84 (µm)	D90 (µm)	D99 (µm)
2010 monsoon daily surface suspended load																								
SNG1	SL	0.68	139	19/05/2010	1.27	-25.7	5.27	-91.4	8.03	-0.39	17.38	6.72	1.31	-1.41	-2.13	17.79	16.99	11	4	6	21	58	75	174
SNG2	SL	0.12	143	23/05/2010			3.22	-98.9																
SNG3	SL	0.7	147	27/05/2010	1.33	-26.4			3.81	-1.51	17.68	2.79	1.02	-1.13	-2.56	17.85	17.22	12	4	6	21	58	76	171
SNG4	SL	0.3	151	31/05/2010	0.90	-24.9	5.32	-91.2										16	3	4	19	100	147	401
SNG5	SL	0.2	152	01/06/2010	0.82	-24.9	2.93	-98.3										16	3	4	20	111	152	298
SNG6	SL	0.25	155	04/06/2010			2.72	-100.4	16.29	-7.88		13.51	2.78	-0.99	-1.28	16.98	17.70	15	3	5	22	124	176	393
SNG7	SL	0.34	159	08/06/2010			2.63	-102.8	19.85	-0.70	17.02	17.47	2.38	-0.66	-0.95	16.92	17.74	20	3	4	14	86	137	334
SNG8	SL	0.49	163	12/06/2010	0.82	-24.4	3.03	-116.9	22.09	-0.40	16.26	19.85	2.24	-0.36	-0.77	16.18	16.95	21	2	4	14	81	132	350
SNG9	SL	0.52	167	16/06/2010	0.53	-24.6	2.62	-107.4	16.05			13.67	2.38		-1.04		16.94	16	3	4	26	253	336	494
SNG10	SL	0.82	168	17/06/2010	0.82	-24.6	2.89	-105.5	16.03	-0.17	16.53	12.87	3.16	-0.13	-0.30	16.22	17.77	22	2	3	13	75	113	310
SNG11	SL	1.75	169	18/06/2010	0.78	-26.5	3.17	-96.1	7.51	-1.51	17.28	4.99	2.52	-1.23	-2.05	17.32	17.19	14	3	5	22	101	142	311
SNG12	SL	1.48	170	19/06/2010	0.76	-25.4	3.21	-95.9	10.09	-0.78	16.26	7.48	2.61	-0.69	-1.05	15.82	17.51	14	3	5	23	139	210	453
SNG13	SL	3.08	171	20/06/2010	1.01	-26.6	3.78	-90.1	7.82	-0.39	17.38	5.04	2.78	-1.20	-1.66	20.33	18.34	21	2	4	13	66	129	364
SNG14	SL	3.69	172	21/06/2010	0.68	-25.3	3.22	-89.5	18.79	-0.64	16.03	14.65	4.14	-0.58	-0.87	15.47	18.03	13	4	6	25	142	220	527
SNG15	SL	2.02	173	22/06/2010	0.49	-25.0												11	4	7	31	146	210	473
SNG16	SL	1.55	174	23/06/2010	0.48	-25.1			15.78	-0.54	17.26	12.99	2.79	-0.43	-1.06	17.21	17.50	14	3	5	25	135	191	364
SNG17	SL	2.19	175	24/06/2010	0.40	-25.1	2.04	-95.3	14.24	-0.44	17.35	11.85	2.39	-0.36	-0.85	17.25	17.81	9	5	9	73	271	304	412
SNG18	SL	1.58	176	25/06/2010	0.59	-24.8			15.25	-0.55	17.09	12.42	2.83	-0.46	-0.93	16.97	17.58	10	4	7	45	261	320	510
SNG19	SL	1.58	177	26/06/2010														14	3	5	27	151	210	394
SNG20	SL	1.73	178	27/06/2010	0.54	-25.0	2.46	-99.7	15.97	-0.43	16.95	12.99	2.98	-0.33	-	16.93	17.06							

														0.87								
SNG21	SL	4.3	179	28/06/2010	0.49	-25.4				-0.93	19.43	9.89		-0.93		19.43		16	3	5	19	77	108	257
SNG22	SL	2.26	180	29/06/2010	0.44	-24.6						14.12	2.47	-0.26	-0.76	16.90	18.55	11	4	7	35	142	182	303
SNG23	SL	2.65	181	30/06/2010	0.44	-24.7												12	4	6	25	98	143	293
SNG24	SL	3.94	182	01/07/2010	0.41	-25.2						10.7	4.01	-0.70	-0.94	17.53	18.08	15	3	5	24	123	167	310
SNG25	SL	3.76	183	02/07/2010	0.49	-25.4	2.32	-95.0	14.29	-0.80	18.25	10.69	3.6	-0.76	-0.91	18.15	18.57	10	5	7	47	184	227	358
SNG26	SL	4.1	184	03/07/2010			1.92	-95.1	10.03	-0.85	17.00	7.64	2.39	-0.82	-0.94	16.99	17.04	5	9	16	71	164	196	314
SNG27	SL	3.3	185	04/07/2010	0.40	-25.4			11.33	-0.87	16.82	8.62	2.71	-0.88	-0.86	17.02	16.20	7	6	10	51	145	180	330
SNG28	SL	3.47	186	05/07/2010	0.44	-25.7			10.65	-0.92	16.48	7.9	2.75	-0.88	-1.06	16.31	16.97	7	7	11	66	236	287	449
SNG29	SL	2.88	188	07/07/2010	0.41	-25.4			10.27	-0.81	16.85	7.55	2.72	-0.74	-1.00	16.73	17.19	10	5	8	40	125	158	277
SNG30	SL	2.29	189	08/07/2010	0.34	-25.2			8.36	-0.72	16.87	5.72	2.64	-0.61	-0.94	16.73	17.16	9	5	8	41	129	164	279
SNG31	SL	1.46	190	09/07/2010	0.36	-24.8	1.87	-96.6	20.4	-0.60	17.80	17.14	3.26	-0.50	-1.10	17.76	18.04	12	4	6	37	138	182	357
SNG32	SL	2.06	191	10/07/2010	0.32	-24.9			19.14	-0.44	17.28	15.9	3.24	-0.37	-0.79	17.15	17.96	10	4	7	47	168	211	376
SNG33	SL	2.13	194	13/07/2010	0.41	-25.1			18.31	-0.76	17.48	14.65	3.66	-0.70	-1.04	17.37	17.93	12	4	6	40	156	199	329
SNG34	SL	3.45	196	15/07/2010	0.69	-25.9				-0.52		5.38	2.09	-0.52	-1.23	14.38	14.02	9	5	7	27	76	100	220
SNG35	SL	2.01	197	16/07/2010	0.42	-25.9			20.7	-0.57	17.30	17.02	3.68	-0.49	-0.92	17.29	17.35	11	4	7	35	130	172	387
SNG36	SL	1.94	199	18/07/2010	0.45	-24.0	2.03	-110.7	24.85	0.02	16.80	21.89	2.96	0.09	-0.56	16.62	18.11	16	3	4	21	86	116	238
SNG37	SL	3.23	200	19/07/2010	0.26	-24.1						13.75	3.23	-0.15	-0.74	16.26	16.98	11	4	7	44	155	196	342
SNG38	SL	7.99	201	20/07/2010	0.51	-24.6	2.51	-107.5	20.14	-0.44	16.70	17.39	2.75	-0.38	-0.83	16.48	18.07	14	3	5	24	87	115	237
SNG39	SL	5.79	202	21/07/2010	0.38	-24.1						16.26	4.67	-0.76		15.82		12	4	6	32	118	157	321
SNG40	SL	3.1	203	22/07/2010	0.45	-24.1				-0.54	17.10	15.9	3.6	-0.54	-0.87	17.10	17.71	13	4	6	29	96	121	216
SNG41	SL	3.52	204	23/07/2010	0.38	-25.5	1.79	-95.9	18.83	-0.62	17.26	14.61	4.22	-0.54	-0.89	17.04	18.01	10	5	8	52	190	244	483
SNG42	SL	3.62	205	24/07/2010	0.30	-24.9						15.03	4.53	-0.65	-1.07	16.36	17.22	11	4	7	39	130	165	294
SNG43	SL	3.57	206	25/07/2010	0.26	-24.2			18.4	-0.54	17.25	13.93	4.47	-0.43	-0.86	16.99	18.07	12	4	6	36	148	191	335
SNG44	SL	5.25	207	26/07/2010	0.31	-24.7				-0.72	16.82	10.65	3.03	-0.72	-1.07	16.82	17.54	10	5	7	31	105	147	300

SNG45	SL	3.98	208	27/07/2010	0.49	-25.2	2.22	-98.3	23.24	-0.72	18.11	19.79	3.45	-0.67	-1.01	18.12	18.03	15	3	5	22	85	113	233
SNG46	SL	4.58	209	28/07/2010	0.26	-24.9						14.62	4.4	-0.50	-0.89	15.88	17.51	10	5	7	50	203	254	431
SNG47	SL	2.47	210	29/07/2010	0.28	-24.7												10	4	7	50	203	260	472
SNG48	SL	5.67	211	30/07/2010	0.31	-25.0				-0.67	17.29	11.99	3.02	-0.67	-0.99	17.29	17.68	7	6	11	55	175	220	353
SNG49	SL	3.24	212	31/07/2010	0.37	-24.9			17.49	-0.74	16.99	12.44	5.05	-0.69	-0.88	16.80	17.46	9	5	8	44	159	206	377
SNG50	SL	4.65	213	01/08/2010	0.25	-24.4				-0.24	16.73	11.96	3.99	-0.24	-0.83	16.73	17.53	8	5	9	62	180	218	352
SNG51	SL	2.17	214	02/08/2010	0.29	-24.2	1.71	-104.6	17.91	-0.31	17.21	14.15	3.76	-0.16	-0.87	16.98	18.09	11	4	7	47	161	199	321
SNG52	SL	3.01	215	03/08/2010	0.51	-25.7												10	5	8	39	136	173	295
SNG53	SL	4.08	216	04/08/2010	0.21	-24.3			14.09	-0.54	16.71	10.68	3.41	-0.40	-0.98	16.55	17.22	6	8	15	98	242	285	434
SNG54	SL	8.04	217	05/08/2010	0.24	-24.6	2.10	-90.3	8.5	-0.87	18.14	6.42	2.08	-0.80	-1.11	18.27	17.73	6	7	12	59	177	223	403
SNG55	SL	4.12	218	06/08/2010	0.23	-24.1			14.41	-0.71	17.47	10.56	3.85	-0.39	-1.61	17.24	18.09	7	6	11	74	212	253	410
SNG56	SL	1.69	219	07/08/2010	0.31	-24.3			18	-0.17	16.62	14.55	3.45	-0.05	-0.67	16.28	18.06	13	4	6	37	141	181	322
SNG57	SL	2.48	220	08/08/2010	0.39	-24.8			16.67	0.03	16.59	13.7	2.97	0.20	-0.79	16.36	17.66	13	4	6	26	90	114	193
SNG58	SL	2.03	221	09/08/2010	0.24	-24.7												10	4	7	37	129	166	295
SNG59	SL	1.75	222	10/08/2010	0.52	-25.7			17.87	-0.16	16.86	14.37	3.5	-0.04	-0.63	16.52	18.27	11	4	7	34	109	140	251
SNG60	SL	2.14	223	11/08/2010	0.42	-24.8			16.1	-0.03	17.47	12.88	3.22	0.28	-1.26	17.34	17.98	12	4	6	31	127	170	314
SNG61	SL	3.04	224	12/08/2010	0.31	-24.3			18.7	-1.02		14.63	4.07	-0.33	-1.31	17.37	18.11	8	5	9	53	162	197	294
SNG62	SL	1.38	225	13/08/2010	0.33	-24.6				-0.53	16.02	19.85		-0.53		16.02		12	4	6	36	136	173	293
SNG63	SL	1.18	226	14/08/2010	0.41	-25.0	2.14	-97.8	21.62	-0.41	17.73	18.19	3.43	-0.32	-0.90	17.68	18.02	12	4	6	30	117	154	298
SNG64	SL	1.43	227	15/08/2010	0.25	-24.5												11	4	7	49	165	205	345
SNG65	SL	3.23	228	16/08/2010	0.29	-25.0			10.15	-0.70	17.59	8.03	2.12	-0.19	-2.63	17.48	18.00	10	5	7	32	95	123	265
SNG66	SL	1.93	229	17/08/2010	0.30	-23.9			19.88	-0.86	17.58	16.94	2.94	-0.71	-1.74	17.52	17.92	11	4	7	38	119	150	279
SNG67	SL	2.17	230	18/08/2010	0.38	-25.4			17.49	-0.55	16.99	14.54	2.95	-0.50	-0.76	16.79	17.95	11	4	7	37	144	186	301
SNG68	SL	2.23	231	19/08/2010	0.40	-24.8	1.99	-109.3	20.3	-0.18	16.93	17.02	3.28	-0.08	-0.67	16.73	17.96	13	4	6	32	124	164	324
SNG69	SL	6.03	232	20/08/2010	0.35	-24.9						13.33	3.01	-0.21	-3.84	16.99	18.33	15	3	5	25	131	193	393

SNG70	SL	3.07	233	21/08/2010	0.34	-24.6			18.82	-0.01	17.17	14.76	4.06	0.21	-0.81	16.85	18.32	14	3	5	28	141	194	403
SNG71	SL	3.74	234	22/08/2010	0.25	-24.4			16.72	-0.12	17.35	13.69	3.03	0.01	-0.72	17.17	18.19	9	5	8	62	217	272	462
SNG72	SL	3.47	235	23/08/2010	0.23	-24.9												7	6	11	78	212	253	425
SNG73	SL	5.07	236	24/08/2010	0.46	-25.8	2.02	-96.1	17.45	-0.61	17.66	14	3.45	-0.49	-1.13	17.64	17.73	10	4	7	47	171	216	365
SNG74	SL	3.62	237	25/08/2010	0.25	-24.9			18.71	-0.28	17.32	14.86	3.85	-0.14	-0.85	17.19	17.82	9	5	9	66	202	244	385
SNG75	SL	3.54	238	26/08/2010	0.31	-24.5												14	3	5	40	268	323	418
SNG76	SL	2.79	239	27/08/2010	0.34	-25.2			18.15	-0.37	17.16	14.26	3.89	-0.22	-0.92	16.83	18.38	7	6	12	95	247	294	443
SNG77	SL	2.81	240	28/08/2010	0.40	-25.6	1.76	-98.1	16.72	-0.45	16.88	12.95	3.77	-0.30	-0.94	16.54	18.03	9	5	9	58	214	273	462
SNG78	SL	4.09	241	29/08/2010	0.19	-24.6												7	6	11	98	274	322	473
SNG79	SL	6.84	242	30/08/2010	0.24	-24.9	1.60	-100.5	16.8	-0.76	17.76	13.31	3.49	-0.51	-1.72	17.76	17.74	7	6	11	100	240	277	420
SNG80	SL	3.96	243	31/08/2010	0.33	-25.3			14.09	-0.61	16.99	10.91	3.18	-0.53	-0.85	16.65	18.15	6	9	17	118	257	292	406
SNG81	SL	2.59	244	01/09/2010	0.24	-24.1												8	6	10	95	252	291	429
SNG82	SL	3.6	245	02/09/2010	0.42	-25.1	2.27	-97.5	13.38	-0.20	16.66	11.52	1.86	-0.11	-0.81	16.51	17.55	9	5	8	56	187	227	339
SNG83	SL	3.21	246	03/09/2010	0.27	-24.6												8	5	9	75	233	281	432
SNG84	SL	3.22	247	04/09/2010	0.38	-25.8												10	4	7	48	192	238	385
SNG85	SL	2.44	248	05/09/2010	0.66	-25.5			23.17	-0.18	17.67	19	4.17	0.14	-1.66	17.51	18.39	12	4	6	41	170	212	355
SNG86	SL	2.13	249	06/09/2010					19.56	-0.06	17.20	15.53	4.03	0.13	-0.78	17.03	17.83	12	4	6	37	168	208	341
SNG87	SL	3.36	250	07/09/2010														9	5	8	46	150	189	333
SNG88	SL	2.62	251	08/09/2010	0.36	-25.2												10	4	7	36	136	181	388
SNG89	SL	1.9	252	09/09/2010	0.31	-25.5			15.88	-0.37	17.37	12.23	3.65	-0.24	-0.79	17.12	18.20	9	5	9	53	176	223	411
SNG90	SL	1.66	253	10/09/2010	0.24	-25.1	1.87	-92.0	15.46	-0.33	17.12	11.54	3.92	-0.15	-0.85	16.94	17.64	9	5	9	52	157	195	314
SNG91	SL	1.38	254	11/09/2010	0.30	-25.4						19.56	3.99	-0.34	-3.16	18.16	18.40	9	5	8	46	144	178	300
SNG92	SL	5.43	255	12/09/2010	0.39	-26.1			14.14	-0.99	18.13	11.03	3.11	-0.96	-1.08	18.16	18.05	8	5	8	36	120	161	336
SNG93	SL	2.42	256	13/09/2010	0.31	-25.8	2.40	-87.6	12.83	-0.87	16.53	9.51	3.32	-0.86	-0.90	16.49	16.65	8	5	9	43	134	171	322
SNG94	SL	2.06	257	14/09/2010					12.56	-0.89	17.37	9.73	2.83	-0.79	-1.21	17.36	17.43	7	7	11	65	197	245	404

SNG95	SL	2.51	258	15/09/2010	0.45	-25.8			12.15	-0.83	16.30	9.13	3.02	-0.81	-0.91	15.99	17.22	8	6	9	44	135	170	294
SNG96	SL	5.68	259	16/09/2010	0.25	-25.5	2.53	-87.6	7.38	-1.42	18.34	5.49	1.89	-1.01	-2.62	18.42	18.12	7	7	11	50	157	205	411
SNG97	SL	2.01	260	17/09/2010	0.31	-25.9												10	5	8	52	183	220	332
SNG98	SL	3.72	261	18/09/2010	0.29	-25.8			7.93	-0.78	16.72	5.04	2.89	-0.70	-0.92	16.33	17.42	8	5	9	43	141	186	355
SNG99	SL	2.41	262	19/09/2010	0.32	-24.9						8.57	2.70	-1.10	-1.10	16.59	16.59	13	4	6	24	84	116	295
SNG100	SL	2.22	263	20/09/2010	0.26	-24.7			13.11	-0.89	16.93	9.58	3.53	-0.79	-1.15	16.59	17.87	9	5	8	44	161	211	379
SNG101	SL	2.85	264	21/09/2010	0.24	-24.7			9.96			6.84	3.12	-0.77	-1.10	16.75	17.64	7	7	11	57	164	205	353
SNG102	SL	1.03	265	22/09/2010	0.30	-25.1			14.26	-0.79	17.38	10.48	3.78	-0.71	-1.00	17.16	18.00	9	5	8	45	143	182	328
SNG103	SL	1.55	266	23/09/2010	0.33	-26.0			13.98			12.18	1.8	-0.81	-1.02	17.96	18.80	7	6	11	69	191	231	362
SNG104	SL	2.04	267	24/09/2010	0.27	-24.9	1.89	-92.5	15.37	-0.99	16.85	11.59	3.78	-0.98	-1.05	16.55	17.77	8	6	10	58	201	246	417
SNG105	SL	1.03	268	25/09/2010	0.30	-25.4			16.9			12.23	4.67	-0.76	-1.09	17.22	18.11	10	5	8	46	149	188	329
SNG106	SL	1.03	269	26/09/2010	0.29	-25.5			15.18	-0.79	16.94	13.77	1.41	-0.77	-1.00	16.86	17.76	8	5	9	59	190	229	360
SNG107	SL	0.9	270	27/09/2010	0.32	-25.1			16.83	-0.85	17.65	15.48	1.35	-0.82	-1.20	17.58	18.40	8	5	9	62	178	214	354
SNG108	SL	0.55	271	28/09/2010	0.44	-25.5			17.58	-1.06	16.96	15.96	1.62	-0.77	-3.90	16.75	19.06	11	4	7	35	112	145	266
SNG109	SL	0.49	272	29/09/2010	0.38	-25.5												11	4	7	40	135	170	287
SNG110	SL	0.54	273	30/09/2010														9	5	9	63	185	226	377
SNG111	SL	0.51	274	01/10/2010	0.32	-25.2	1.86	-99.6	16.08	-0.85	16.62	12.39	3.69	-0.80	-1.03	16.13	18.26	8	5	9	71	220	271	451
SNG112	SL	0.45	275	02/10/2010	0.37	-25.6			15.95	-1.16	17.71	11.98	3.97	-0.59	-2.87	17.52	18.29	7	6	11	83	219	272	446
SNG113	SL	0.38	276	03/10/2010														8	5	9	62	209	267	487
SNG114	SL	0.45	277	04/10/2010	0.29	-25.4			14.11	-1.26	17.79	10.5	3.61	-0.66	-3.01	17.57	18.41	7	7	12	101	276	318	459
SNG115	SL	0.26	278	05/10/2010														10	4	7	39	129	166	304
SNG116	SL	0.29	279	06/10/2010	0.43	-26.0												7	6	11	76	202	242	393
SNG117	SL	0.3	280	07/10/2010														7	7	12	85	224	265	421
SNG118	SL	0.28	281	08/10/2010														7	7	12	77	211	256	399
SNG119	SL	0.57	282	09/10/2010	0.55	-26.0	1.91	-100.6	12.89	-1.37	17.76	9.86	3.03	-0.92	-2.84	17.64	18.17	4	11	20	96	231	276	430

SNG120	SL	0.38	283	10/10/2010													5	10	18	110	270	318	477
SNG121	SL	0.33	284	11/10/2010	0.31	-25.4											4	13	25	137	295	342	513
SNG122	SL	0.29	285	12/10/2010	0.30	-25.7			14.4	-1.67	17.89	10.72	3.68	-0.78	-4.29	17.66	18.55	4	12	24	145	298	343	506
SNG123	SL	0.21	286	13/10/2010														4	12	22	124	288	332	481
SNG124	SL	0.17	287	14/10/2010														6	8	14	82	214	259	422
SNG125	SL	0.37	288	15/10/2010	0.24	-25.5												2	25	49	183	324	361	489
2005 depth profiles																								
PB 60	SL 0	2.59	192	11/07/2005	0.34	-24.5																		
PB 58	SL 0	2.92	192	11/07/2005	0.33	-24.7	1.97	-96.0	21.75			16.15	5.6	-0.55		17.07	-13.42	13	4	5	22	74	97	207
PB 57	SL 2	4.81	192	11/07/2005	0.24	-24.3	1.59	-95.1				14.73		-0.64		17.05	-13.45	9	5	8	44	123	150	303
PB 56	SL 4	5.59	192	11/07/2005	0.21	-24.3	1.47	-96.2				13.87		-0.63		17.14	-13.35	4	9	14	77	171	210	425
PB 55	SL 6	9.10	192	11/07/2005	0.20	-24.3	1.39	-97.2	17.22			12.57	4.65	-0.68	-0.89	17.15	-13.34	5	8	13	71	180	222	416
PB 54	SL 8	10.24	192	11/07/2005	0.18	-24.2	1.26	-96.7	16.3			11.7	4.6	-0.71	-1.09	17.14	-13.36	3	11	20	102	235	281	452
2007 depth profiles																								
LO 757	SL 0	1.46	224	12/08/2007	0.28	-24.4	1.68	-101.5	22.5	-0.33	17.38	18.33	4.17	-0.23	-0.78	17.33	17.62							
LO 756	SL 3.3	1.64	224	12/08/2007	0.21	-24.0	1.61	-103.4	20.1	-0.33	17.38	16.32	3.78	-0.26	-0.62	17.29	17.77							
LO 754	SL 6	2.22	224	12/08/2007	0.21	-23.9	1.46	-101.5	17.23	-0.39	17.38	13.68	3.55	-0.33	-0.64	17.26	17.86							
LO 755	SL 8	1.79	224	12/08/2007	0.29	-24.0	1.61	-102.8	17.84	-0.39	17.37	14.31	3.53	-0.34	-0.61	17.30	17.67							
LO 758 A	SL 7.5	1.27	224	12/08/2007	0.36	-24.4	1.84	-103.0																
LO 758 B	SL 8	1.64	224	12/08/2007	0.30	-24.1	1.62	-102.1																
LO 758 C	SL 8.5	30.90	224	12/08/2007	0.16	-25.3	0.98	-97.9																
2011 depth profiles																								
CA11117	SL 0	2.18	216	04/08/2011	0.44	-25.3	2.57	-94.0										13	4	6	26	83	107	206
CA11118	SL 2.3	3.40	216	04/08/2011	0.31	-25.0	1.99	-92.0										8	6	9	54	182	229	377
CA11116	SL 5.5	3.70	216	04/08/2011	0.26	-25.0	2.01	-92.1										8	5	9	53	193	239	384
CA11119	SL 8.5	3.63	216	04/08/2011	0.26	-25.5	1.89	-92.1										7	6	11	69	223	271	404
CA11123	SL 0	1.73	217	05/08/2011	0.37	-25.0	2.25	-96.0										12	4	6	29	103	142	384

CA11124	SL 2	2.56	217	05/08/2011	0.30	-25.5	1.86	-93.1	8	5	9	61	197	239	370
CA11122	SL 5.5	3.65	217	05/08/2011	0.20	-25.2	1.66	-88.3	6	7	13	98	241	283	423
CA11121	SL 9.3	5.99	217	05/08/2011	0.20	-25.4	1.45	-95.6	4	13	27	166	344	395	584
CA11127	SL 0	4.05	218	06/08/2011	0.51	-25.4	2.30	-95.9	13	4	6	30	103	133	276
CA11126	SL 3	4.49	218	06/08/2011	0.43	-25.3	2.00	-96.2	10	5	7	46	162	205	364
CA11125	SL 5	5.37	218	06/08/2011	0.35	-24.9	1.89	-90.1	10	5	8	50	175	222	373
CA11128	SL 8	6.67	218	06/08/2011	0.30	-25.1	1.67	-99.7	7	7	13	107	281	327	472
CA11130	SL 0	3.97	218	06/08/2011	0.40	-24.6	2.15	-102.9	11	4	7	39	139	179	352
CA11131	SL 2	5.11	218	06/08/2011	0.42	-25.8	2.00	-97.9	10	5	8	53	172	213	369
CA11129	SL 6.3	5.59	218	07/08/2011	0.38	-25.3	1.95	-95.8	9	5	9	62	189	228	359

Cs: sediment concentration; SL: Suspended Load; TOC: Total Organic Carbon; Calc.: calcite; Dol.: dolomite; Carb.: carbonate; Cont.: content in weight percent; D10, 16, 50, 84, 90, and 99 respectively represent the particle diameters of 10th, 16th, 50th, 84th, 90th, and 99th percentiles in the cumulative grain size distribution.

Table 2: Annual sediment flux estimates (see text and supporting information S7 for details on the four methods).

Method	flux estimate	Hydrological timescale resolution	k coefficient	*Qs* Total sediment flux [Mt/yr]	Equivalent erosion rate [mm/yr] [#]
DMC0	*measured Cs (no Cs depth gradient)*	*daily*		*108*	*1.28*
DMC	measured *Cs*	daily		153 ± 15	1.80 ± 0.18
HCC	$Cs = k_1 \cdot Qd$	hourly*	constant	152 ± 16	1.80 ± 0.19
HQCc	$Qs = k_2 \cdot Qd$	hourly*	constant	158 ± 16	1.86 ± 0.2
HQCv	$Qs = k_2(t) \cdot$ Qd	hourly*	9-day sliding average	140 ± 15	1.65 ± 0.18
		*daily data used before 17 May and after 30 November 2010.			[#]using rock density of 2.65 g/cm^3

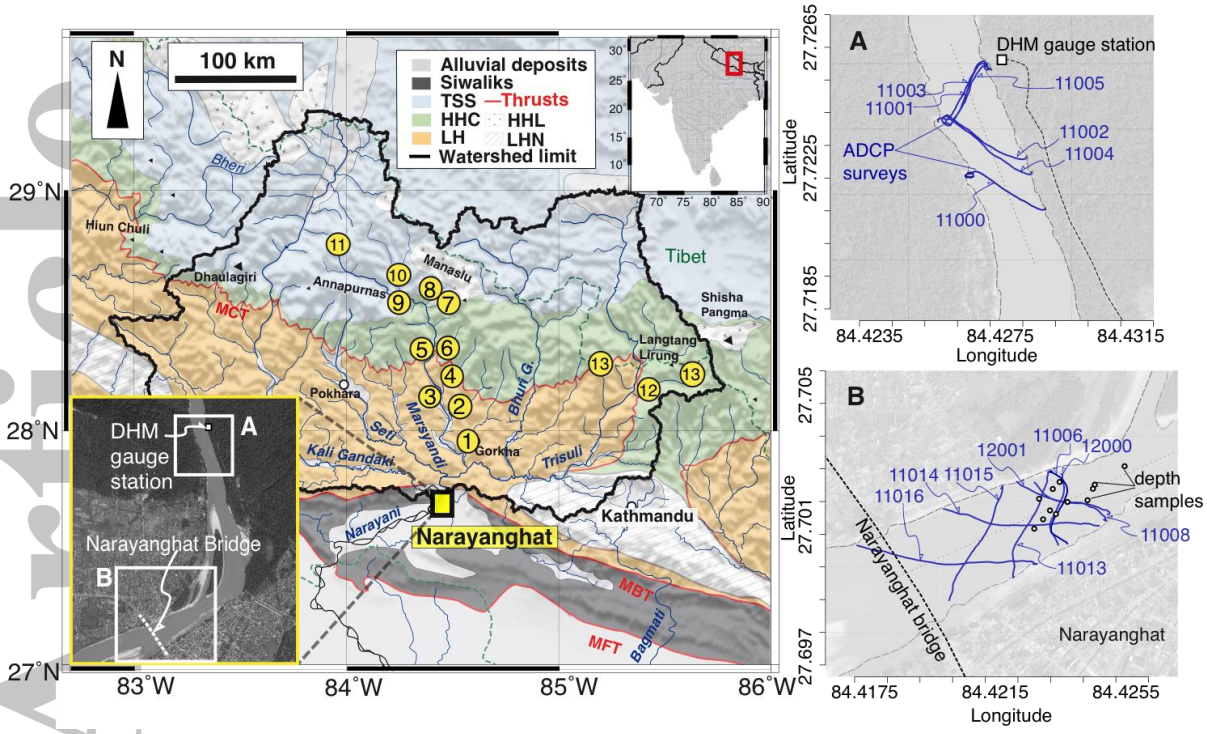

Figure 1: Geographic setting of the Narayani River and its tributaries. The Narayani basin (outlined by the thick black line) drains 32,000 km^2 of the central Nepal Himalayan range. Daily surface suspended sediment sampling was performed from the middle of Narayanghat bridge (Narayanghat–Bhâratpur, Nepal) in 2010. The outset maps show ADCP measurement lines (blue lines) and depth sampling points (dots) near the DHM (Department of Hydrology and Meterorology of Nepal) gauge station ~3 km upstream of the Narayanghat bridge (A) and just upstream of the bridge (B). Yellow dots represent the main confluences of the Marsyandi River with tributaries that were sampled for this study: 1: Darondi, 2: Chepe, 3: Paudi, 4: Dordi, 5: Khudi, 6: Ngadi, 7: Dudh and Dudh glaciers, 8: Dona; 9: Ghatte, 10: Naur, 11: the Marsyandi River source, 12: Langtang, 13: Langtang glaciers, 14: Mailung.

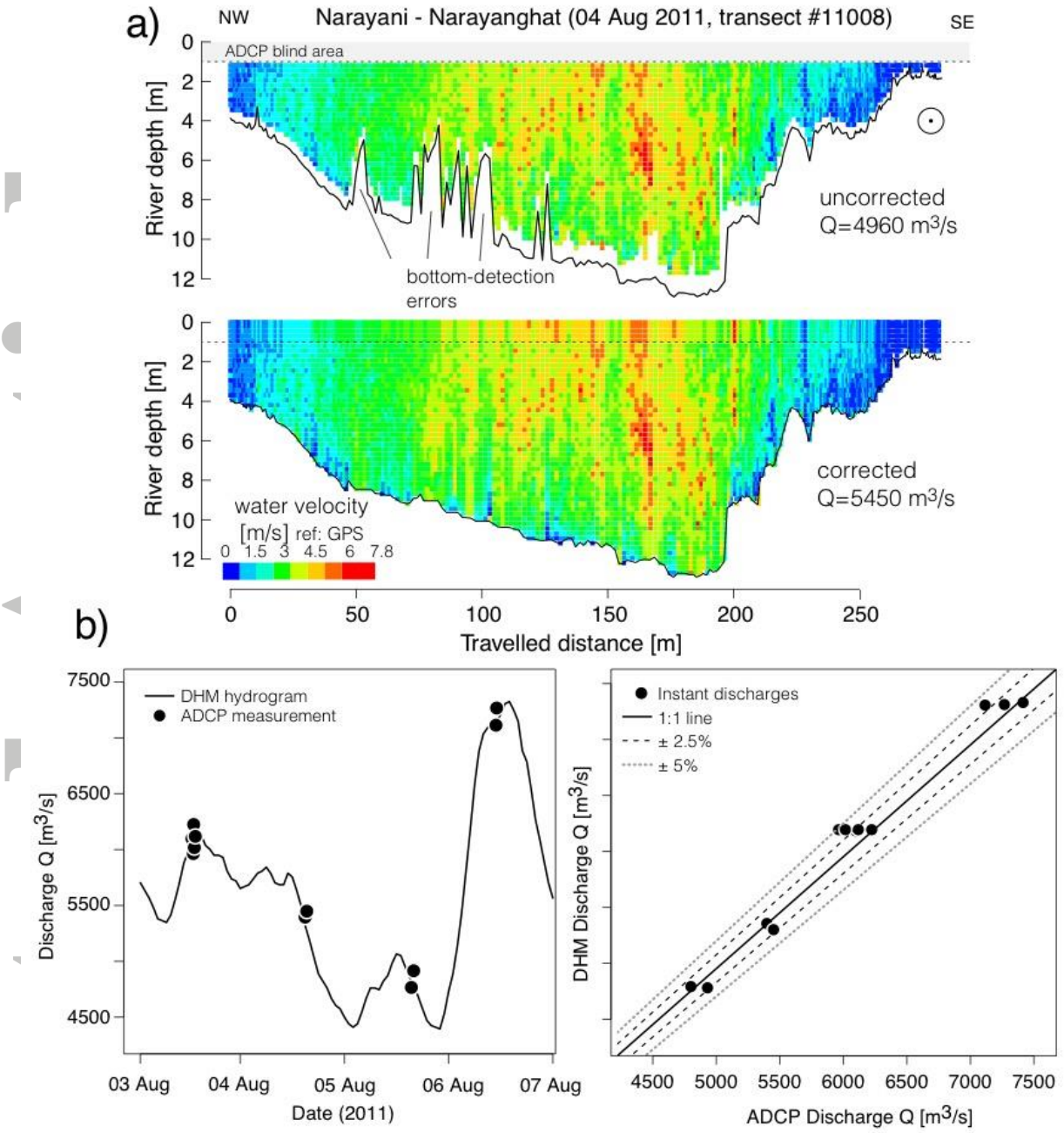

Figure 2: (a) Comparison between raw/uncorrected (top) and corrected/extended (bottom) ADCP measurement (transect #11008). The x-axis represents the distance travelled by the boat. Errors in the river bottom topography (blanks/spikes in the uncorrected section) were corrected and water velocities above the ADCP blind area and along the channel bottom were extrapolated by fitting the existing velocity data. Water velocities can reach ~7.8 m/s in the central part of the channel. The river flows to the SW in this section. (b) Comparison between corrected ADCP instant discharges and continuous discharges reported by Department of Hydrology and Meteorology from water level data during 4–7 August 2011 (left). The ADCP discharge values show good agreement with DHM (Department of Hydrology and Meterorology of Nepal) estimates: all errors are within 5% and most within 2.5% (linear regression: $Q_{DHM} = 1.008 \cdot Q_{ADCP}$ with $r^2 = 0.9996$; right). See supporting Figure S2 for more details.

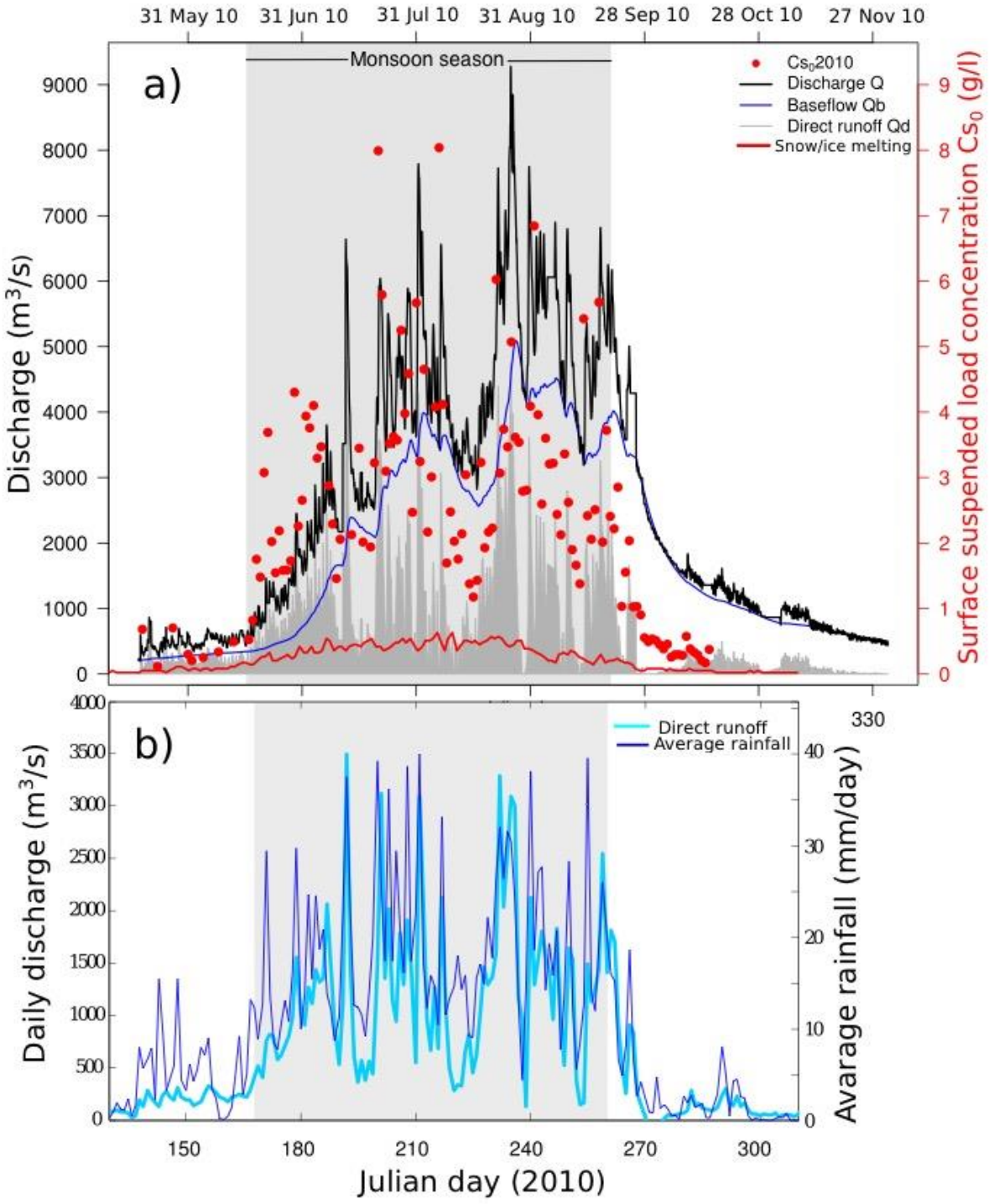

Figure 3: (a) Hourly Narayani River discharge hydrograph (black line) and surface sediment concentration Cs_0 (red dots) during the 2010 monsoon. Increased discharges (> 1,000 m^3/s) and sediment concentrations (> 1 g/L) are observed at the beginning of the monsoon in mid-June (~Julian day 166) and remain elevated until mid-September (~Julian day 259). This coeval pattern demonstrates the first order climatic control of monsoons over erosion, i.e., sediment production/transport. The general coherence between Cs_0 and discharge peaks indicates the probable effects of rainstorms on sediment delivery to the river drainage. Narayani discharge *Q* (black line), groundwater component *Qb* (blue line), and direct runoff

component *Qd* (shaded grey) were calculated with a modified numerical filter after (Andermann et al., 2012a; Eckhardt, 2005, 2008).

(b) During the monsoon, the direct runoff component *Qd* (light blue) agrees well with the average daily precipitation in the Narayani watershed (dark blue) and the snow/ice-melt flux (red) derived from the positive degree day model.

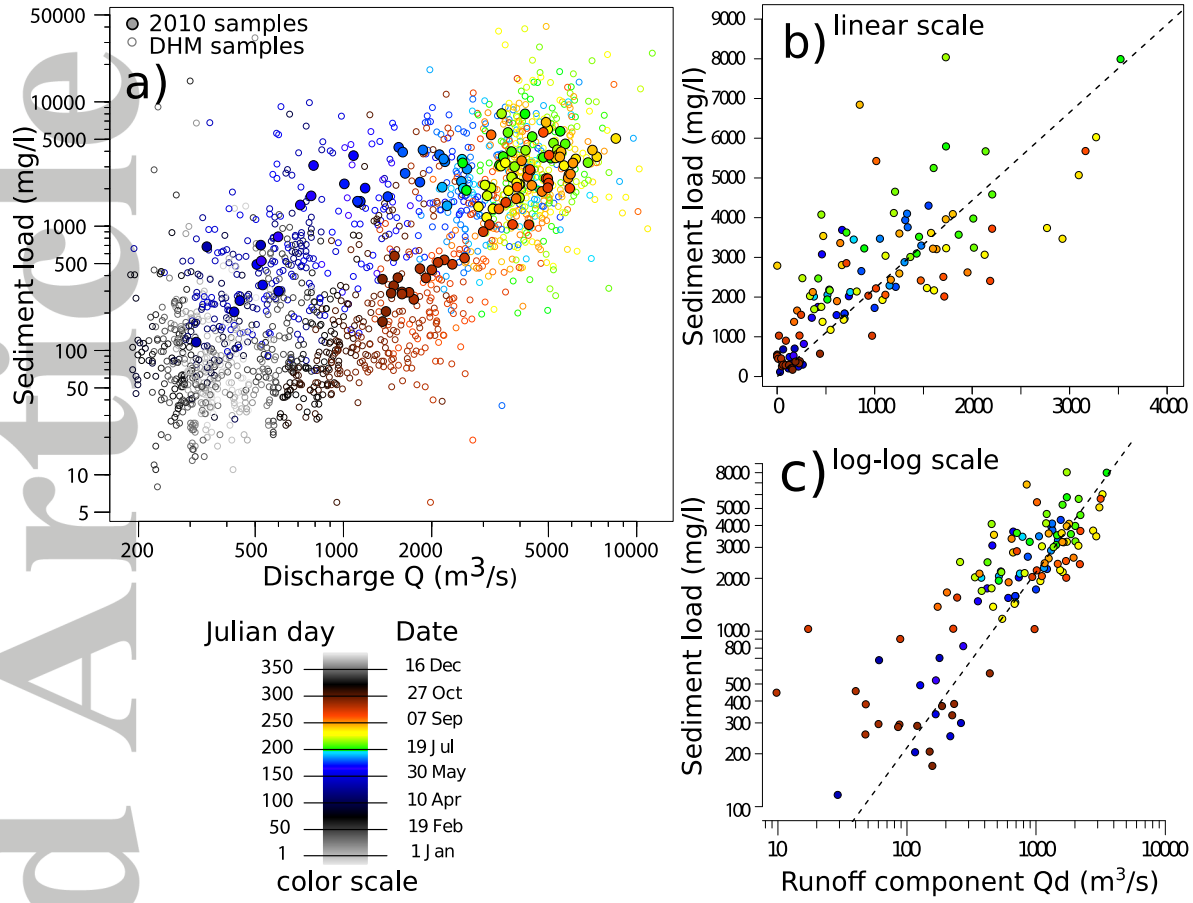

Figure 4: (a) Narayani surface suspended sediment concentrations Cs_0 relative to river discharge Q (log-log scale). DHM Cs_0 historical chronicles are represented by open symbols, and Cs_0 measured at the Narayanghat bridge in 2010 by filled symbols. 2010 samples span the period from 18 May to 14 October (Julian days 138–287) and follow the yearly clockwise hysteresis loop observed in the DHM chronicles.

(b) Cs_0 compared to direct runoff Qd in 2010. As in (a), the symbol color corresponds to the date between late May and mid-October. The dashed line corresponds to the mean linear relation between Cs and Qd. (c) Same as (b) but in log-log scale to highlight premonsoon and postmonsoon values.

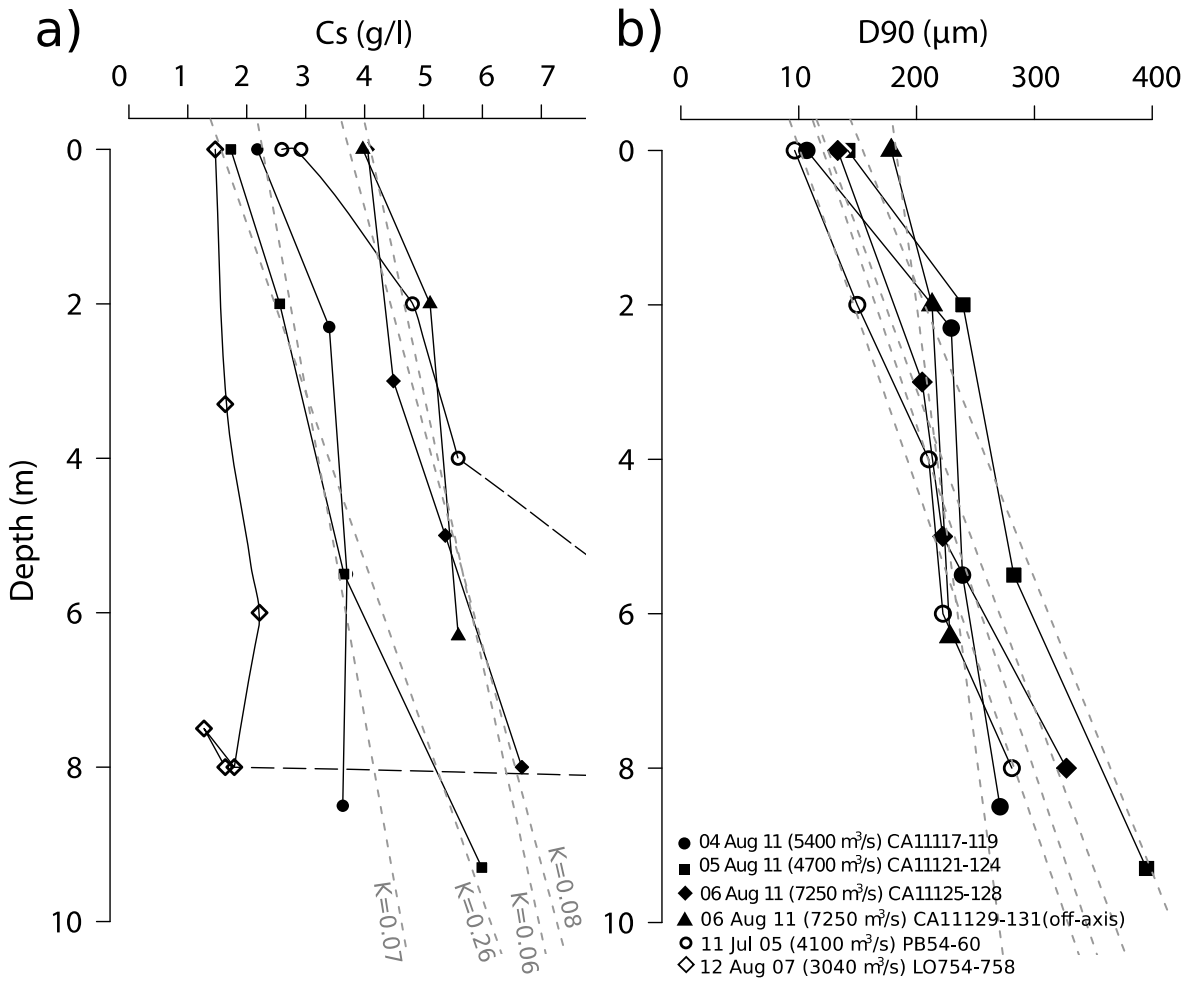

Figure 5: Vertical profiles of (a) suspended sediment concentration *Cs* and (b) grain size (represented by D90) measured by depth sampling along the Narayani River water column in 2005, 2007, and 2011. Both *Cs* and D90 increase linearly with depth, and K values express *Cs* increase with depth as expressed in eq. 1. Bedload samples from 2005 and 2007 (samples PB and LO, respectively) plot beyond the display area in (a), and are connected to their respective profiles by heavy dashed lines.

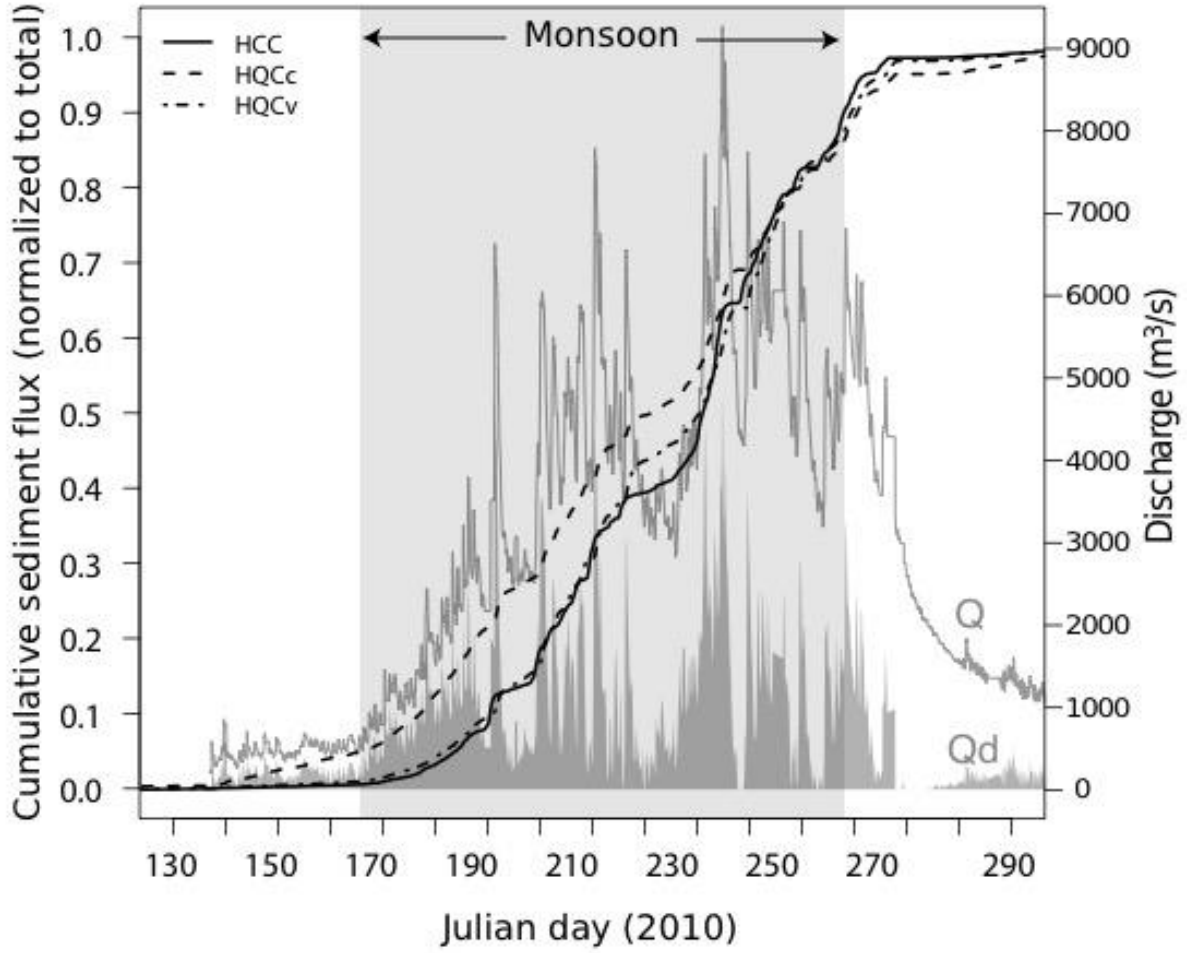

Figure 6: Cumulative sediment fluxes obtained by different methods of integration over the year 2010 (see Table 2 for the total sediment budget). Sediment fluxes *Qs* correspond to 1) case HCC, solid line: the product of *Cs* and the discharge *Q*, with *Cs* determined from the linear regression with direct runoff *Qd*; 2) case HQCc, dashed line: *Qs* determined from the instantaneous *Qd* based on a constant relationship between *Qs* and *Qd* over the entire year; and 3) case HQCv, dash-dotted line: *Qs* determined from the instantaneous *Qd*, applying a 9-day sliding average relationship between *Qs* and *Qd*. Narayani discharge is in grey curve and direct runoff *Qd* is in shaded area.

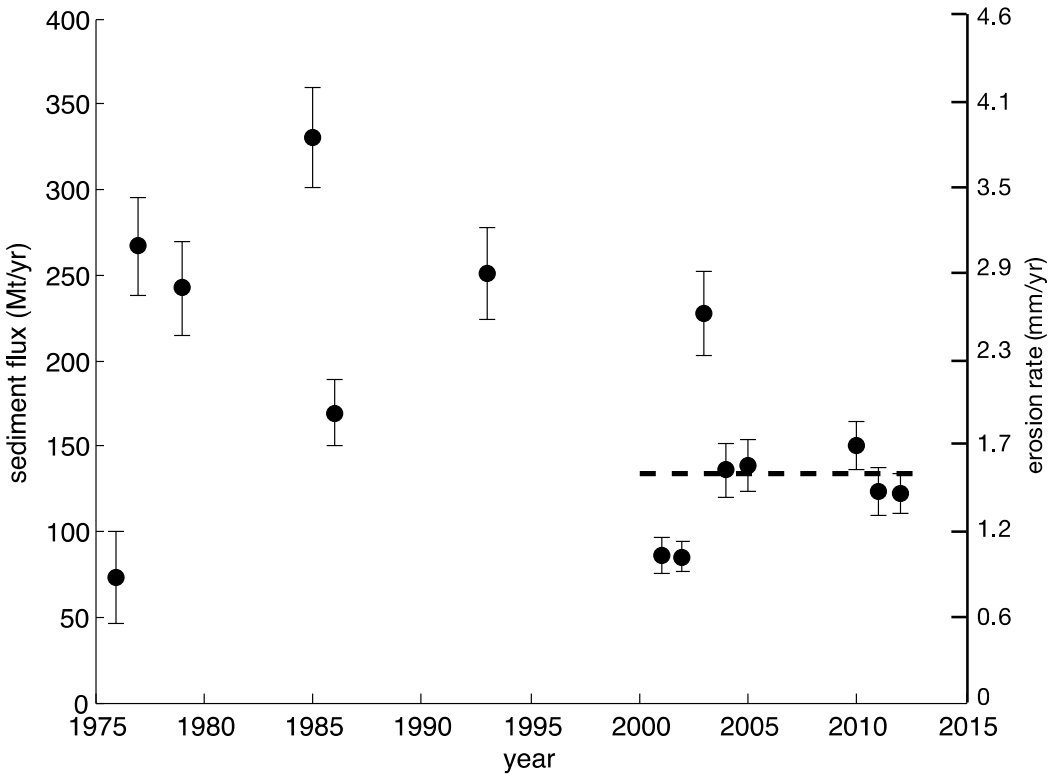

Figure 7: Annual sediment flux and equivalent erosion rate derived from DHM daily suspended load data over 14 noncontiguous years. The average flux of 135 Mt/yr (dashed line) was calculated only for records after the year 2000 (see text for justification).

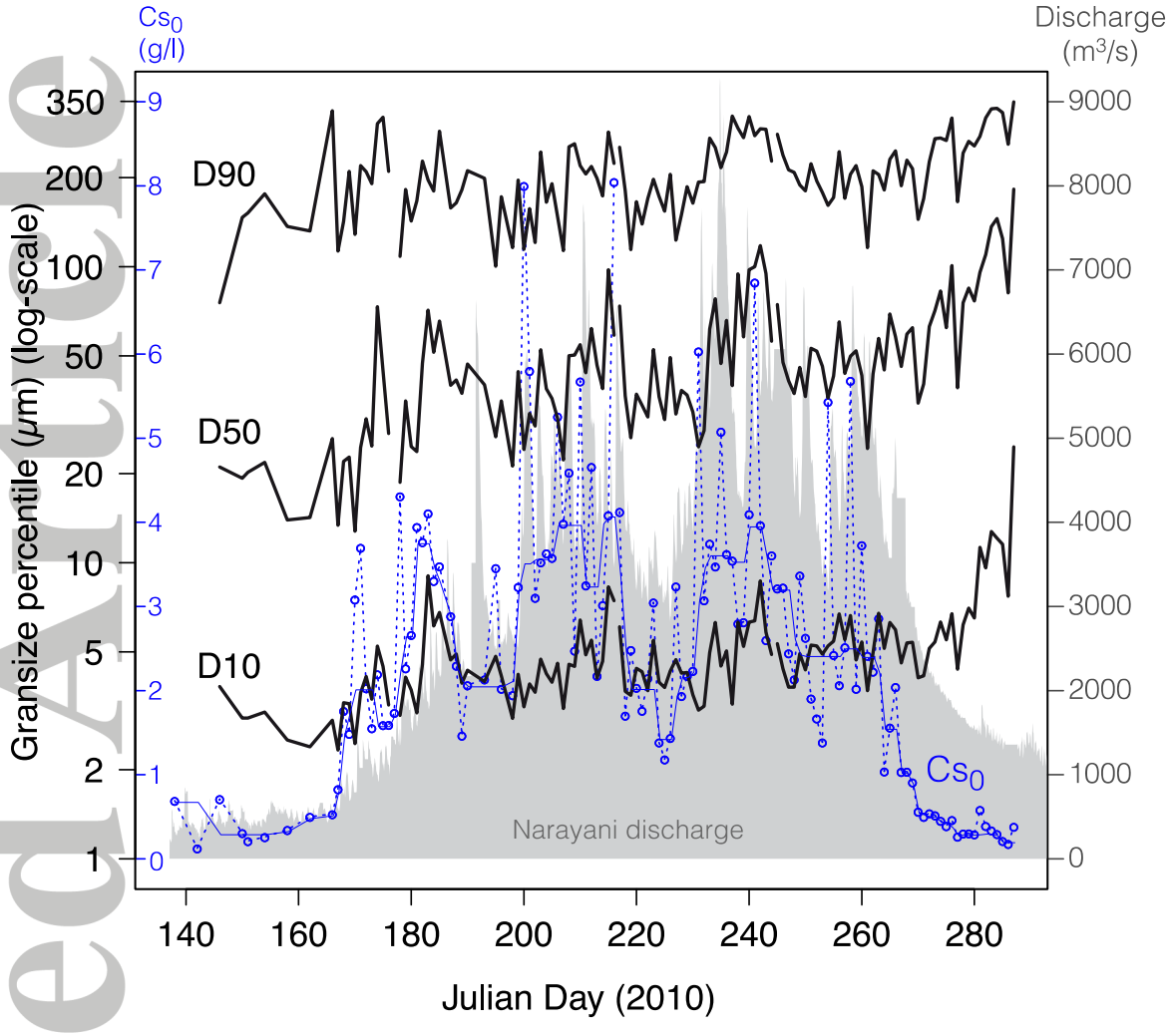

Figure 8: Evolution of the grain size distribution of surface suspended sediments during the 2010 monsoon. D10, D50, and D90 correspond respectively to the 10th, 50th, and 90th percentiles of the bulk sediment grain size distribution. Surface sediment concentrations Cs_0 are represented by blue circles and their smoothed evolution by the blue line. The shaded area corresponds to the hourly Narayani River discharge.

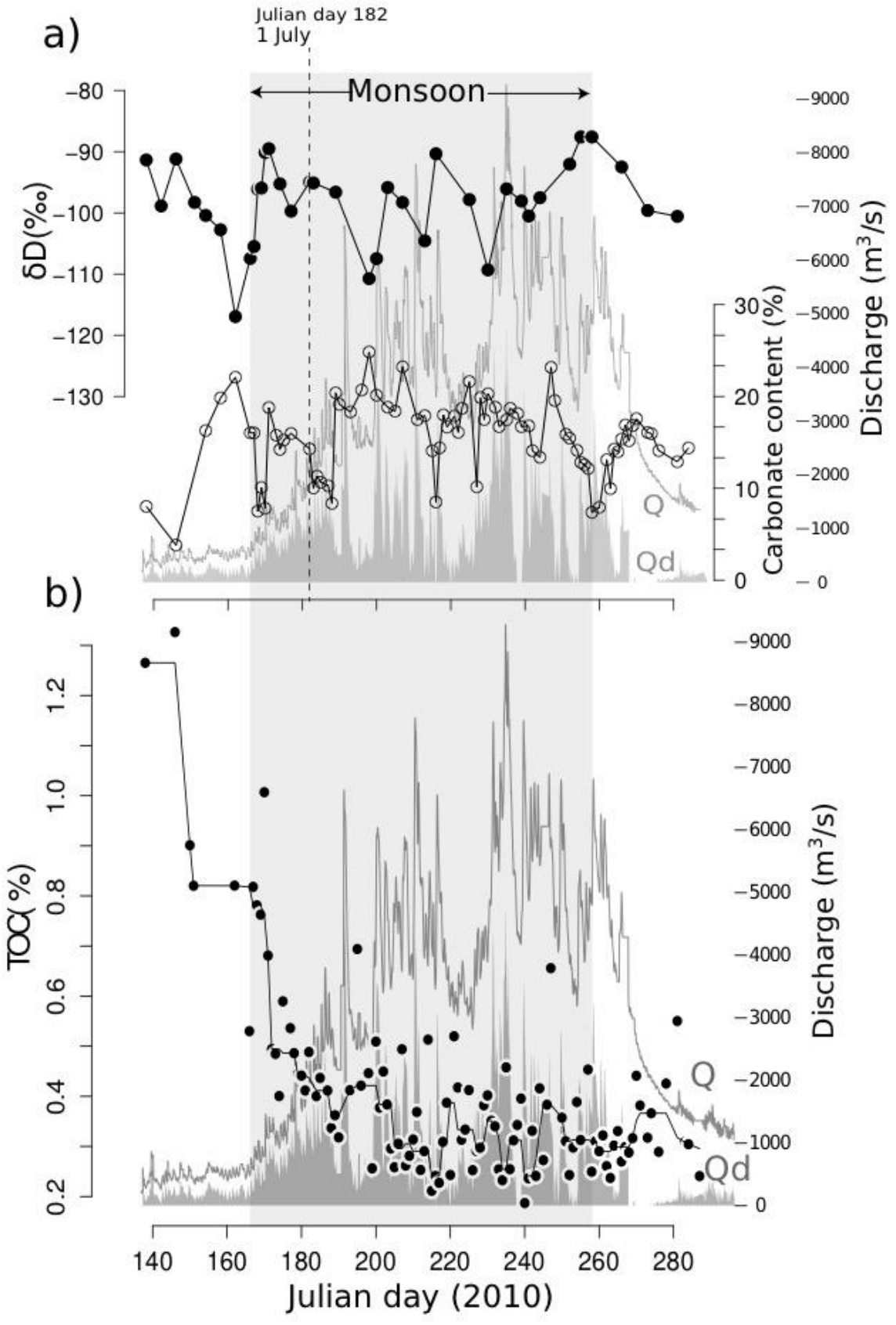

Figure 9: (a) Time series of Narayani surface suspended sediment carbonate content and δD values during the 2010 monsoon. The two series display a rough anticorrelation. (b) The time

series of Total Organic Carbon (TOC) content shows a marked decrease at the beginning of the monsoon (before Julian day 180) interpreted as the vanishing yield of soil erosion in the Narayani sediments.

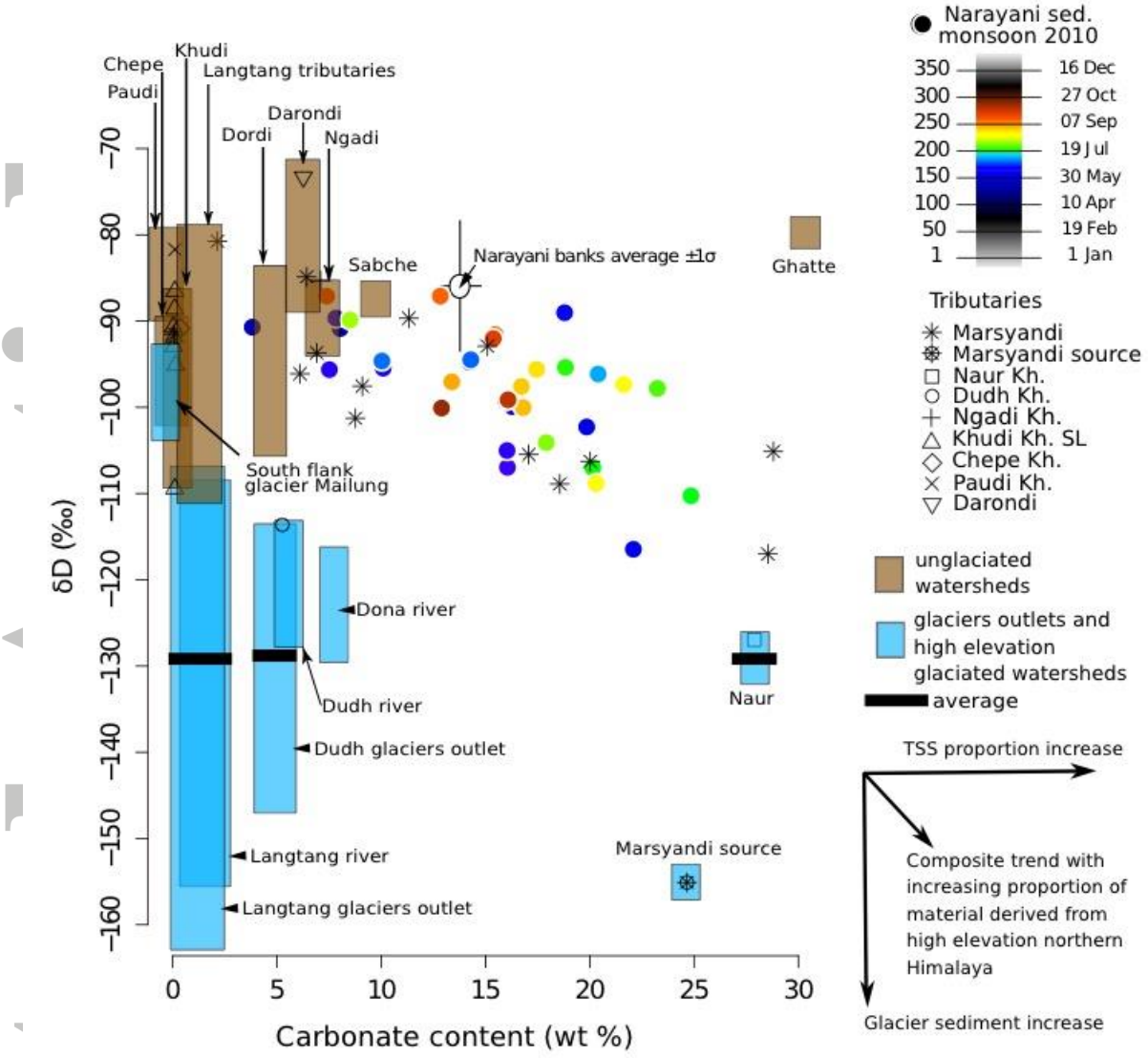

Figure 10: Carbonate content versus δD values of suspended load sediments in the Narayani River during 2010, the Marsyandi River, and Marsyandi tributaries. The anticorrelation of both tracers indicates that sediments derived from the northern flank basin have high carbonate contents and TSS proportions, and are hydrated by water that is depleted in D relative to high altitude and glacial weathering environments. Sediment compositions from small Marsyandi tributaries demonstrate the two end members: northern glaciated basins (Dudh, Dona, Naur Kh., Marsyandi source) with low δD values and/or high carbonate contents, and southern nonglaciated basins (Ngadi, Khudi, Chepe, Paudi, Dordi, Darondi Kh.) showing less negative δD values and low carbonate contents. Sediments sampled from the Marsyandi and Narayani Rivers demonstrate mixing of sediments from the two source regions. Monsoonal Narayani sediments do not display any general temporal evolution during the monsoon. See Figure 1 for locations.

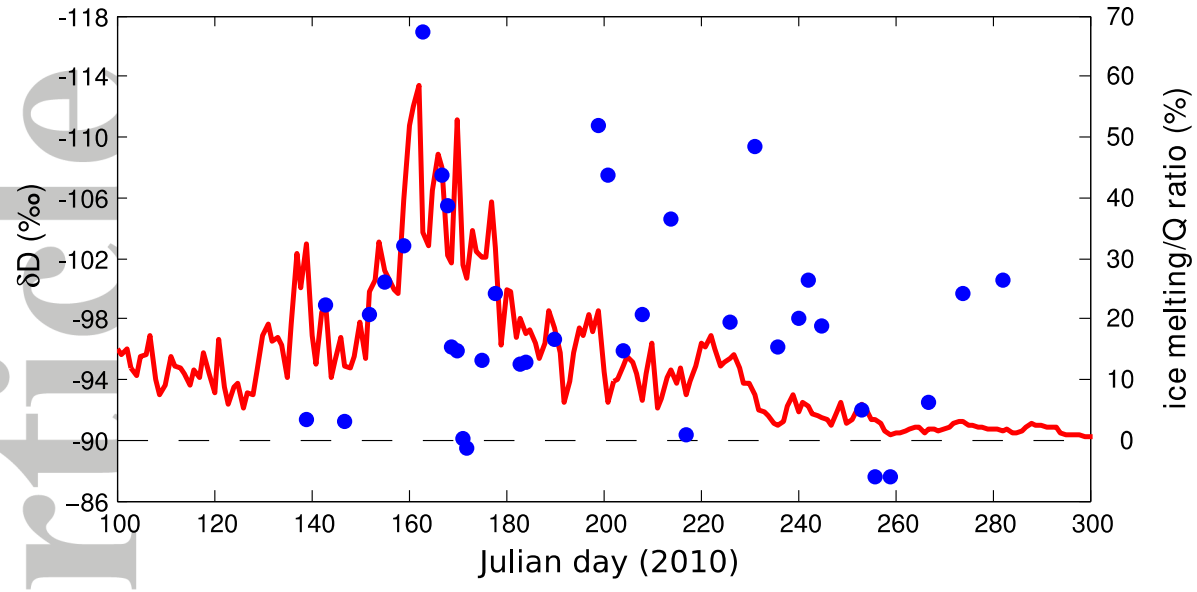

Figure 11: δD values of hydrated silicates in the Narayani suspended load (blue dots) superimposed on the relative contribution of ice melting to the Narayani River discharge (red line). Ice melting was computed using a Positive Degree Model (Rana et al., 1996) from daily temperatures recorded at 10 DHM weather stations in the High Himalaya.

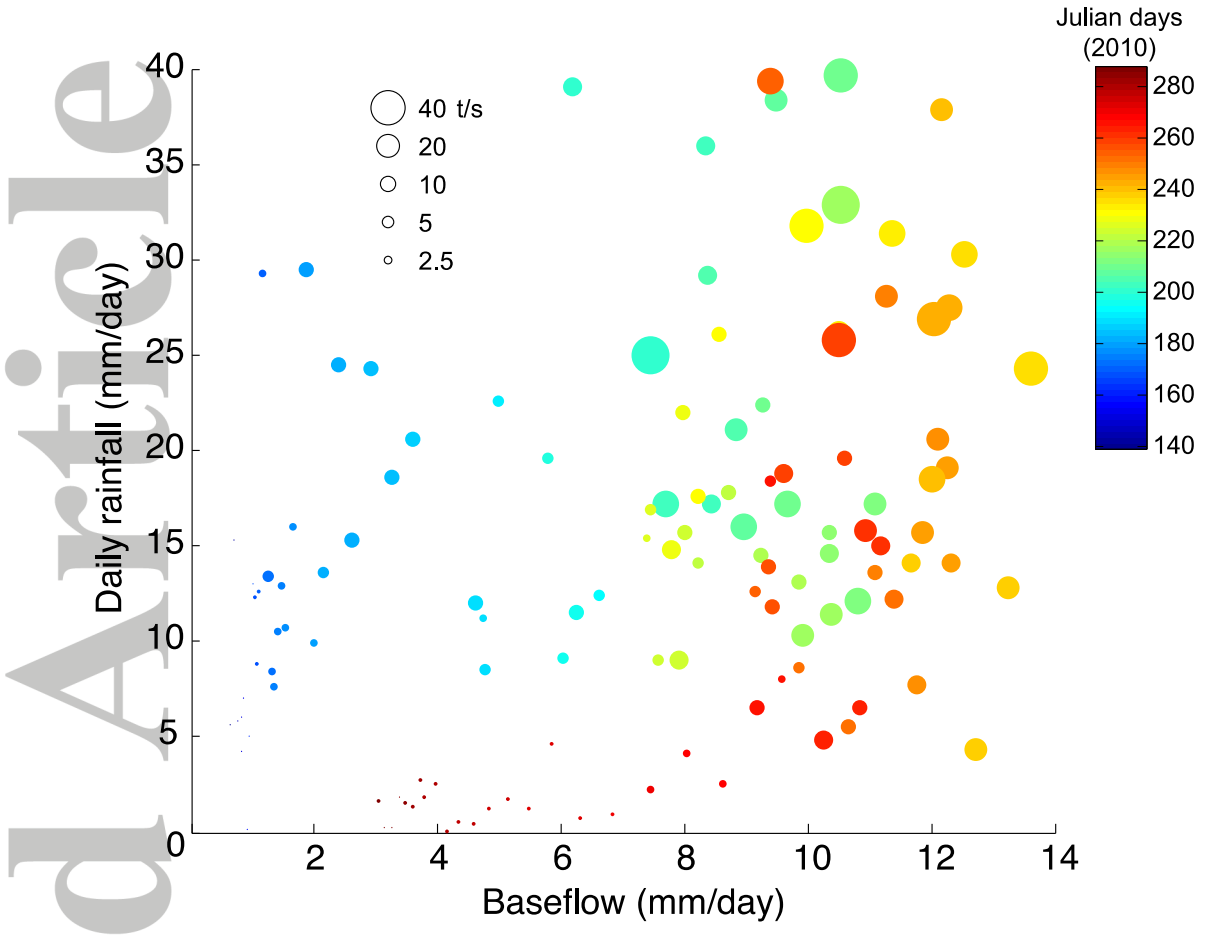

Figure 12: Daily sediment flux as a function of groundwater baseflow and daily rainfall. Symbol size is proportional to sediment flux, and the dashed grey lines segregate spaces of similar sediment yields. Symbol colors represent the Julian day.

Appendix A: Hydrodynamic considerations for sediment flux calculation

A.1 Water velocity depth-profile

Integration of the suspended sediment flux through an entire wetted river section requires a description of the water velocity over that section, assuming that the suspended load is moving jointly with the water, i.e., with similar horizontal velocity.

The water velocity depth-profile is controlled by the bottom roughness z_0 and the velocity $u(z)$ at elevation ζ above the local channel bottom, and can be expressed using the widely used law of the wall (Eq. A1a) (Garcia, 2008):

$$\frac{u_{(z)}}{u^*} = \frac{1}{\kappa}\ln\left(\frac{\zeta}{z_0}\right), \quad \text{(A1a)}$$

or as a function of the depth below the surface z:

$$\frac{u(x,z)}{u*} = \frac{1}{k}\ln\left(\frac{30(z_B(x) - z)}{k_s}\right), \quad \text{(A1b)}$$

where u^* is the shear velocity related to the average boundary shear stress τ_b such that $u^* = (\tau_b/\rho)^{1/2}$, κ the von Karman constant, $z_B(x)$ the local bottom depth counted from the water surface, $z_0 = k_s/30$ the bottom grain-scale roughness, and k_s the effective roughness height, here defined by $3 \times D_{50} = 0.22$ m from pebble median sizes measured on local Narayani gravel bars (Mezaki & Yabiku, 1984; M Attal & Lavé, 2006; Dingle et al., 2016). In theory, such an equation is only considered valid for the lowest part (~1/3) of the water column, but following (Sime et al., 2007) we apply it to the entire water column.

A.2. Energy slope S_e

In the above equation, deriving the vertical velocity profile requires computing u^*, i.e., $\tau_b = \rho \cdot g \cdot H \cdot S_e$, where ρ is the fluid density, g the gravity constant taken at 9.8 m/s^2, and S_e the energy slope, which is expected to depend on the flow stage. An empirical determination between discharge Q and surface slope $S_e = u^{*2}/g \cdot H$ can be established for 2011 from the results of ADCP integrations, using the equation of the law of the wall integrated along the water column in uniform regimes (Wilcock, 1996) (c.f. Eq. A2):

$$u^* = <U> \cdot k \cdot \ln\left(\frac{h}{e \cdot z_0}\right), \quad \text{(A2)}$$

where $<U>$ is the depth-averaged velocity, h the water depth (m), and e the natural logarithmic base. We used equation (A2) to compute shear velocity u^* from velocity profiles

measured by ADCP for each position along the transects, and u^* is then averaged for each transect. This method proved to provide a better estimate of u^* from ADCP data than direct fitting of the law of the wall (Lupker et al., 2011a; Sime et al., 2007).

The so-obtained energy slope seems almost constant along the transect in supporting figure S7A, at around 0.05% for discharge values ranging between 5,000 and 5,500 m^3/s, but significantly departs from the energy slope calculated further downstream at sections 11014–11016, which are close to the mean regional channel gradient at Narayanghat, i.e. ~0.11%. Because the channel widens downstream, and because the downstream transects are relatively more oblique and therefore less suitable for deriving a local slope, it is difficult to include these latter results to derive a relation for $S_e = f(Q)$ that is valid for both clusters of points.

In the absence of additional data to constrain the energy slope for discharge values well below or above ~5,000 m^3/s in the section of supporting figure S7A, we followed a conservative hypothesis considering the energy slope as remaining roughly constant at ~0.05%, regardless of the water discharge (solid line on Fig. S7B). This value was used to compute the water flux by considering double integrating over the channel area horizontally on $W(H)$ and vertically on the water column defined between $k_s/30$ (bottom) and $H–z_B(x)$ (surface) as follows:

$$Q = \sqrt{S_e(Q)}\frac{\sqrt{g}}{k}\int_0^{W(H)}\sqrt{H - z_B(x)}\int_{k_s/30}^{H-z_B(x)}\ln\left(\frac{30z}{k_s}\right)dz\,dx \quad . \qquad \text{(A3)}$$

This calculation provides a direct relation between H and Q at the studied section, i.e., a rating curve $H = f(Q)$ at the Narayanghat Synthetic River Section (Fig. S7A). This rating curve allows us to compute the water depth for any DHM-reported discharge value further upstream, and to use the linear increase of the suspended load concentration with depth to compute sediment flux at any time, as long as the section in figure S7A has remained unchanged.

To further test the influence of our simplifying hypothesis of a constant energy slope, we tested another scenario in which the energy slope depends on discharge following a power law with an exponent of 0.6. This relation (dashed line on Fig. S7B) is expected where the channel progressively widens downstream at Narayanghat (~50 m/km of channel length). If the rating curve obtained through this distinct hypothesis significantly differs from that derived for a constant energy slope, we note that it would have a minor effect (<3% difference) on the annual sediment flux calculation because larger sediment fluxes at

discharges below 5,000 m^3/s are roughly compensated by lower estimates at higher discharge values.